Electronic Supplementary Information

A robust Ni single atom catalyst for Industrial Current and Exceptional Selectivity in Electrochemical CO₂ Reduction to CO

*Zhicheng Liu, [a b] Longsheng Cao, [a *] Manli Wang, [a b] Yun Zhao, [a] Ming Hou, [a *] and Zhigang Shao [a *]*

[a] Fuel Cell System and Engineering Laboratory, Key Laboratory of Fuel Cell & Hybrid Power Sources, Dalian Institute of Chemical Physics, Chinese Academy of Sciences, Dalian, Liaoning, 116023, China

[b] University of Chinese Academy of Sciences, Beijing, 100049, China

* Corresponding authors.

Email addresses: caolsh@dicp.ac.cn, houming@dicp.ac.cn, zhgshao@dicp.ac.cn

Experimental Section

Materials

All chemicals were of analytical pure and used without additional purification. Aniline (99.5%), pyrrole (99%), and ammonium persulphate (99.99%) were purchased from Aladdin Aldrich (Shanghai, China). Triton X-100 was acquired from Solarbio (Beijing, China). Nickel nitrate (98.0%) was from Damao Chemical (Tianjin, China), and Nitric acid (65%~68%) was obtained from Xilong Chemical (Guangzhou, China), respectively. Potassium hydroxide (95%) and potassium bicarbonate (99.99%) were supplied by Macklin (Shanghai, China). Nafion®115 membrane and 5wt.% Nafion® solution were from Dupont® (USA). The resistivity of deionized water used in our experiment was 18.2 MΩ cm^{-1}.

Synthesis of catalysts

Synthesis of polyaniline-co-polypyrrole (PACP)

PACP hollow spheres were fabricated according to the previous literature[1]. In a typical process, 0.38 ml aniline, 0.29 ml pyrrole, and 0.06 g Triton X-100 were sequentially added to 60 ml deionized water. After stirring for 30 min, the homogeneous solution was formed. In the following, the 15 ml deionized water containing 1.9 g ammonium persulphate (APS) was added into the above solution and stirred at 1000 rpm for 60 s. Then, the above solution stands at 0 °C for 12 h without agitation in a programmable temperature and humidity tester. Finally, the product was washed with deionized water until the filtrate became colorless and freeze-dried for 24 h, obtaining PACP.

Preparation of HCNs and activated HCNs-xh

In brief, the HCNs were fabricated by carbonizing PACP under the Ar (99.999%) atmosphere, and HCNs-xh were obtained through activating HCNs under the CO_2 (99.999%) atmosphere. In a typical protocol, 2 g PACPs were pyrolyzed at 800 °C for two hours under Ar flow in the tube furnace. After cooling to room temperature, the obtained HCNs were weighed to calculate yield. Similarly, 2 g HCNs were activated at 900 °C for x hours (x=1,3,5,7) under CO_2 flow. Finally, the activated HCNs were obtained and named HCNs-xh (x=1,3,5,7). The mass of HCNs-xh was also recorded to

calculate the yield of HCNs at different activation times.

Synthesis of Ni-N-HCNs and Ni-N-HCNs-xh

The preparation process of Ni-N-HCNs-xh was divided into three steps: oxidation of HCNs-xh, followed by ion adsorption and pyrolysis under the inert atmosphere. In a typical case, 0.3 g HCNs-xh was dispersed in 100 ml 16 M HNO_3 solution and refluxed at 80 °C for four hours. The resulting product was washed several times with deionized water until the filtrate was neutral, followed by drying in a vacuum oven at 60 °C overnight. We named the product as O-HCNs-xh (x=1, 3, 5, and 7). 0.15 g O-HCNs-xh was introduced into 150 ml deionized water and sonicated for at least 30 min to acquire a homogeneous solution. The 50 ml deionized water containing 0.25 g nickel nitrate was dropwise introduced into the above O-HCNs-xh dispersion and stirred at 600 rpm for 12 h to fully adsorb metal Ni^{2+}. By filtration and vacuum drying, the Ni^{2+}-O-HCNs-xh powder was achieved. Finally, the as-obtained Ni^{2+}-O-HCNs-xh powder was mechanically mixed with C_3N_4, which was prepared by pyrolyzing melamine at 550 °C under an air atmosphere for four hours, with a mass ratio of 1:15, and then heated at 800 °C for one hour under N_2 flow, achieving the catalysts denoted as Ni-N-HCNs-xh (x=1,3,5,7). Similarly, the Ni-N-HCNs were yielded by replacing HCNs with HCNs-xh. Ni-N-HCNs-5h-10 and Ni-N-HCNs-5h-20 were prepared similarly, except the mass ratio of Ni^{2+}-O-HCNs-5h and C_3N_4 was 1:10 and 1:20, respectively. Ni-N-HCNs-5h-700 °C and Ni-N-HCNs-5h-900 °C were acquired by altering the annealing temperature to 700 °C and 900 °C.

Electrochemical measurement

preparation of working electrode:

The gas diffusion layer (GDL) containing a microporous layer was adopted to prepare the working electrode. Typically, 20 mg of the as-prepared catalysts (Ni-N-HCNs-xh) and 100 μL 5% Nafion solution were added to 2ml isopropanol and sonicated for at least 60 min to obtain the catalyst ink. By hand painting, we deposited the catalyst slurry onto the GDL (2.0 cm×2.0 cm). The catalyst loading can be calculated by comparing the quality difference of GDL before and after brushing ink. The catalyst loading was 1.5±0.1 mg cm⁻² for all catalysts when evaluating performance in an H-

cell. For turnover frequency (TOF) determination, a much lower loading (0.1mg cm^{-2} for Ni-N-HCNs-5h) was used to ensure all the catalysts on the working electrode were fully utilized in ECR to CO. For the flow cell test, PTFE was introduced into the working electrode to avoid flooding in the cathode, and the mass ratio of PTFE was 35 wt.%. To avoid the influence of uneven catalyst distribution on the performance of the flow cell, we used automatic spraying to prepare the working electrode. The catalyst loading was set as 2.2±0.1mg cm^{-2}.

Electrochemical CO$_2$ reduction in an H-type cell

Electrochemical measurements were performed in a gas-tight H-type cell, separated by a proton exchange membrane (Nafion 115), as shown in Fig. S2. The electrolyte in the cathode and anode chamber was all 40 ml 0.5M KHCO$_3$ solution. The GDL painted with catalysts was used as the working electrode. Ag/AgCl and Pt plate (2.0 cm×2.0 cm) were used as reference and counter electrodes. CHI760E (CH, China) and Gamry 1000E (Gamry, USA) were used as electrochemical workstations. High-purity CO$_2$ (99.999%) with a flow rate of 60 sccm was continuously purged into electrolytes for at least one hour to make CO$_2$ saturated. When evaluating the electrochemical performance, the flow rate of CO$_2$ was adjusted to 19 sccm. All potentials in the H-cell test were measured against the reference electrode and converted to the RHE reference using E (vs. RHE) =E (vs. Ag/AgCl) +0.198+0.0591×pH, and the PH of CO$_2$ and Ar-saturated 0.5 M KHCO$_3$ solution is 7.2 and 8.3, respectively. Before testing the activity, 20 cycles of cyclic voltammetry (CV) were used to activate the catalysts and make the catalyst's performance reach the best. Linear sweep voltammetry (LSV) was performed in Ar-saturated and CO$_2$-saturated 0.5 M KHCO$_3$ solution with a scan rate of 50 mV^{-1}, and CO$_2$ electroreduction performance of catalysts at different potentials were evaluated by using chronoamperometry (CA) for 20 min at each potential. Stirring (800 rpm) was used to accelerate the mass transfer of the cathode chamber during the measurement. The Tafel plot was acquired from the chronoamperometry results.

The stability test of Ni-N-HCNs-5h in H-cell was conducted at -0.9V/RHE, and the electrolyte was refreshed every 10 to 12 hours to eliminate the effect of concentration

variation in KHCO$_3$ solution on the performance. After the stability test, the electrode was first used to measure the wettability through the contact angle test, and some part of the electrode was used for XPS measurement. Sonicate the electrode in the ethanol to obtain the catalyst dispersion used for HRTEM measurement.

The electrochemical active surface area (ECSA) of Ni-N-HCNs-xh was measured from double-layer capacitance (Cdl) using CV in the potential range between 0.44V and 0.54V (vs. RHE) with various scan speeds of 20, 40, 60, 80, and 100 mV s^{-1}. By determining the ΔJ/2 at 0.49V (vs. RHE) against the scan rate, the Cdl was obtained from the slope. To remove the contribution of GDL on the Cdl, the glassy carbon electrode (GCE) instead of GDL was used as substrate. Specifically, 3 mg of Ni-N-HCNs-xh and 30 µL 5 wt.% Nafion was dispersed in 270 µL isopropanol and sonicated for at least 60 min to obtain a homogeneous catalyst ink. Finally, 3 µL ink was dropped on the GCE, whose area was 0.19625 cm^2, to achieve a catalyst loading of ~ 0.15 mg cm^{-2}. During the test process, three-electrode system (GCE as working electrode, Ag/AgCl as reference electrode, and Pt plate as counter electrode) was used in N$_2$ saturated 0.5 M KHCO$_3$ solution. Before each test, ten cycles of CV were employed to activate the catalyst.

Electrochemical CO$_2$ reduction in a flow cell

Electrochemical measurements were performed in a three-part micro flow cell using chronopotentiometry (CP), as shown in Fig. 6a. The catalysts sprayed GDE was used as cathode with a size of 1.5 cm×1.5 cm. Hg/HgO (1.0 M KOH) and Nickel foam (0.4 mm thickness, 1.5 cm×1.5 cm) sprayed with Ir black were used as reference and anode, respectively. The inlet flow rate of CO$_2$ was controlled at 40 sccm by a mass flow controller, and a mass flowmeter measured the cathode outlet. The flow rate of electrolyte (1M KOH) circulated in the cathode was 5 ml min^{-1}, while in the anode was 15 ml min^{-1}. All potentials in the flow cell test were measured against the Hg/HgO reference electrode and converted to the RHE using E (vs. RHE) =E (vs. Hg/HgO) +0.098+0.0591×pH, and the PH of 1M KOH solution is 14. The stability test in the flow cell was conducted at 100 mA cm^{-2} using CA mode, and the circulated electrolyte, both in the cathode and anode, should be exchanged every hour to eliminate the impact of

KOH concentration changes on the stability test.

Product analysis and evaluation of TOF

The gas products were detected with an online gas chromatograph (Shimazu GC-2014C) equipped with a thermal conductivity detector (TCD) and a flame ionization detector (FID) with a methane conversion furnace (MTN), in which TCD was mainly used to quantify H_2 content. FID was used to quantify CO concentration and any other alkane species. The chromatography is calibrated regularly using standard gases of different concentrations (CO: 198.35, 795.63, and 9980 ppm; H2: 311.95, 1010, and 50100 ppm). The liquid products were examined on a Bruker AVANCE III 600MHz nuclear magnetic resonance (NMR) spectrometer using DSS as an internal standard. Typically, 0.5 ml of electrolyte after electrolysis was mixed with 0.1 ml D_2O containing 0.05 wt.% 1-Propanesulfonic acid 3-(trimethylsilyl) sodium salt (DSS) as internal standard species.

The faradaic efficiency of products (CO and H_2) was calculated as follows:

$$FE_x = \frac{n \times F \times z}{Q} \times 100\% = \frac{1.013 \times 10^{-7} \times F \times v \times n \times N_i}{8.314 \times T \times 60 \times I_{total}} \times 100\%$$

Where,

F: faradaic constant, which is 96458, C mol^{-1};

v: the flow rate of CO_2, which is 19 sccm in H-cell, while the alkaline electrolyte in the flow cell consumes CO_2, the flow rate at the cathode outlet was used to calculate the FE;

n: the number of electrons transferred CO_2 to a given product, which is 2 for CO and H_2;

N_i: the concentration of gas product detected by gas chromatograph, ppm;

T: the ambient temperature, K;

I_{total}: the total current, A.

Similarly, the partial current density was calculated as follows:

$$J_x = \frac{FE_x \times I_{total} \times 1000}{s}$$

Where,

FE_x: faradaic efficiency of CO or H_2;

I_{total}: the total current, A;

S: the geometric surface area of the working electrode involved in measurement, cm^2.

The TOF for CO production was calculated as follows:

$$TOF = \frac{J_{CO}/(n \times F \times 1000)}{m_{CAT}/1000 \times w/M_{Ni}} \times 3600$$

Where,

J_{CO}: CO partial current density, mA cm-2;

n: the number of electrons transferred for CO production, which is 2 for CO;

F: faradaic constant, which is 96458, C mol^{-1};

m_{CAT}: the catalyst loading in the electrode, mg cm^{-2};

w: the content of Ni in the catalyst, which is measured by ICP-OES, wt.%;

M_{Ni}: the atomic mass of Ni, which is 58.69 g mol^{-1}.

It must be mentioned that the sum of FE for CO and H_2 in our work was not exactly 100%, which usually fluctuates between 95% and 115%, as shown in **Table S1**. The deviation comes from the chromatograph quantification error, the bubbles sticking to the electrode surface, etc. To compare the ECR performance between various catalysts, the total FE for each catalyst was normalized to 100%. The catalytic activity data, including FE, J, and TOF, in both H-cell and flow cell, are the average values obtained from three independent tests. Thus, the error bar is just the standard deviations (Mean±SD) in our work.

Physical characterization

The nitrogen adsorption-desorption of HCNs-xh, O-HCNs-xh, and Ni-N-HCNs-xh were investigated by Quantachrome autosorb iQ2 system at 77K. Samples were dehydrated at 300 °C for six hours under vacuum to remove any contaminants on the surface or inside the hole before nitrogen physisorption measurement. The specific surface areas of samples were determined by the multi-point Brunauer-Emmett-Teller (BET) method. Pore size distribution plots were calculated by the Discrete-Fourier-Transformation (DFT) method, and the computed mode is N_2 at 77K on carbon (slit/cylinder, pores, QSDFT adsorption branch). The CO_2 adsorption isotherms were

investigated using the micromeritics TriStar II 3020 system at 298.15K. The samples were outgassed at 300 °C for six hours before measurements. CO_2 temperature-programmed desorption (CO_2-TPD) profiles were obtained from Tianjin Xian Quan TP 5080-B.

The morphologies of catalysts and supports were obtained from scanning electron microscopy (FE-SEM, JSM-7800F) with an accelerating voltage of 1.0 kV. Transmission electron microscopy (TEM) and High-resolution TEM (HRTEM) were conducted on the FEI Tecnai G2 F30 with an accelerating voltage of 300 kV. High-angle annular dark field-scanning transmission electron microscopy (HAADF-STEM) was obtained from JEM-ARM200F (high-resolution images) and FEI Tecnai G2 F30 (low-resolution images). Energy dispersive X-ray spectroscopy images were obtained from AMETEK PV97-61730-ME.

The X-ray absorption spectra (XAS), including X-ray absorption near-edge structure (XANES) and extended X-ray absorption fine structure (EXAFS) of the sample at Ni K-edge, were collected at the Beamline of TLS07A1 in National Synchrotron Radiation Research Center (NSRRC), Taiwan. For Wavelet Transform analysis, the $\chi(k)$ exported from Athena was imported into the Hama Fortran code.[2] The parameters were listed as follows: R-range, 1-4.0 Å, k-range, 0-13.0 Å^{-1} for sample and Standards; k weight, 2; and Morlet function with κ=6, σ=1 was used as the mother wavelet to provide the overall distribution. The XAFS data were processed according to the standard procedures using the Athena module implemented in the IFEFFIT software packages. The EXAFS spectra were obtained by subtracting the post-edge background from the overall absorption and then normalizing concerning the edge-jump step. Subsequently, the $\chi(k)$ data were Fourier transformed to real (R) space using Kaiser-Bessel windows (dk = 1.0 Å^{-1}) to separate the EXAFS contributions from different coordination shells. To obtain the quantitative structural parameters around central atoms, least-squares curve parameter fitting was performed using the ARTEMIS module of the IFEFFIT software packages.[3, 4]

The crystal structure of HCNs-xh and Ni-N-HCNs-xh were obtained using X-ray diffraction (XRD, Empyrean-100 with a Cu Kα radiation source) ranging from 10 ° to 90

°. X-ray photoelectron spectroscopy (XPS) measurements were performed on the Thermo Scientific ESCALAB 250Xi spectrometer using 300 W Al Kα radiation to reveal the surface properties of catalysts and the quantitative analysis of C, N, Ni, and other elements. The binding energies of all elements were calibrated according to the C1s line with peak intensity at 284.8 eV. Raman spectroscopy was performed by the Renishaw NanoWizard instrument with a laser source of 532 nm. The static contact angle was obtained by the KRUSS DSA100 instrument to characterize the wettability of the gas diffusion electrode before and after the stability test.

DFT calculations

The first-principle calculation was performed in the framework of density functional theory as implemented in the VASP program.[5] The generalized gradient approximation proposed by Perdew, Burke, and Ernzerhof is selected for the exchange-correlation potential.[6]The energy criterion is set to 10^{-5} eV in the iterative solution of the Kohn-Sham equation. For all models, the vacuum space along the z-direction was set to be 15 Å, enough to avoid interaction between the two neighboring images. The Brillouin zone integration is performed using a 2×2×1 k-mesh, and a cutoff energy of 450 eV was employed. All the structures are relaxed until the residual forces on the atoms have declined to less than 0.02 eV/Å. The Van der Waals dispersion-corrected DFT was also carried out, as proposed by Grimme.[7]The Gibbs free energy diagrams were estimated by the following equation:

$$\Delta G_i = \Delta E + \Delta ZPE - T\Delta S$$

where ΔE is the energy difference from reactants to products, obtained from DFT calculations; ΔZPE and ΔS are the contributions to the free energy from the zero-point vibration energy and entropy, respectively. T is 298.15 K

The Poisson-Boltzmann implicit solvation model with a dielectric constant of e = 80 for water was used to simulate the H_2O solvent environment
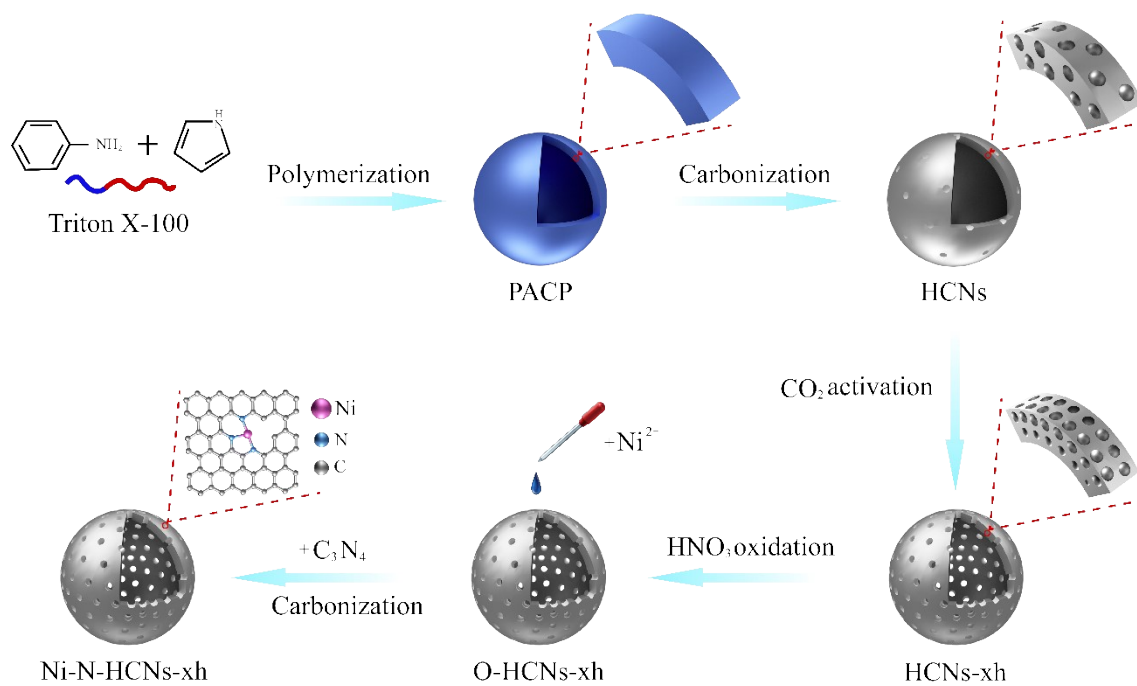
Supplementary Figures and Tables

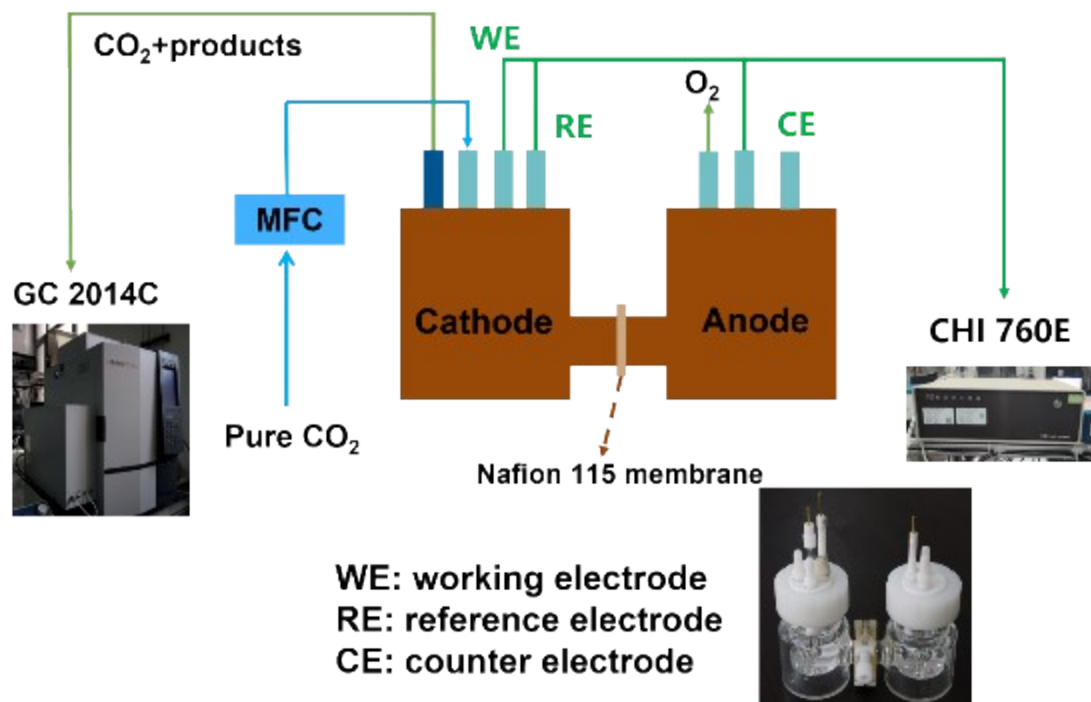**Fig. S1. Schematic illustration of the synthesis process for Ni-N-HCNs-xh catalyst.**

Fig. S2. Schematic illustration and digital photograph of the gas-tight H-type cell for the CO_2 reduction reaction.
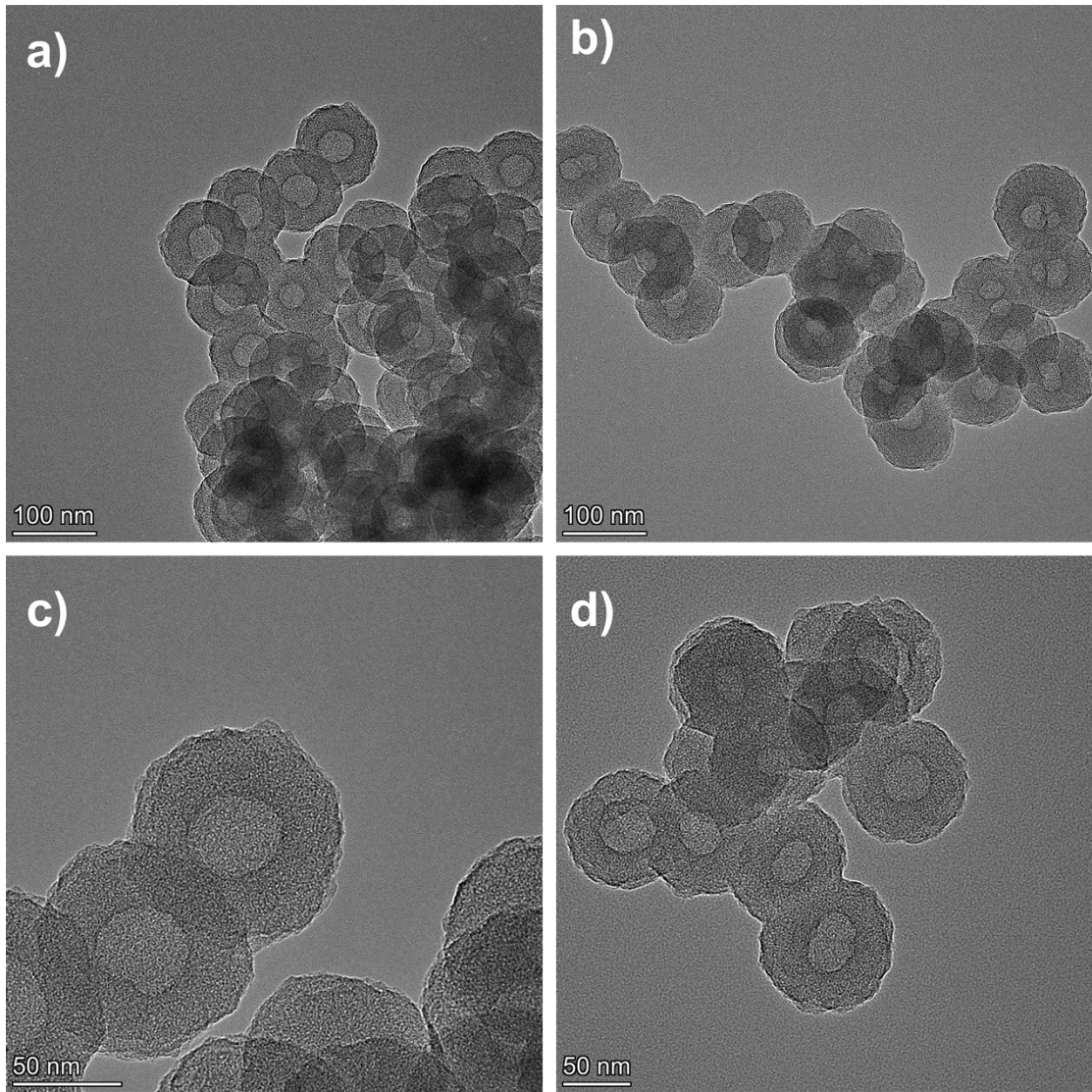
Fig. S3. a) b) c) and d) TEM images of HCNs at different magnifications and regions.
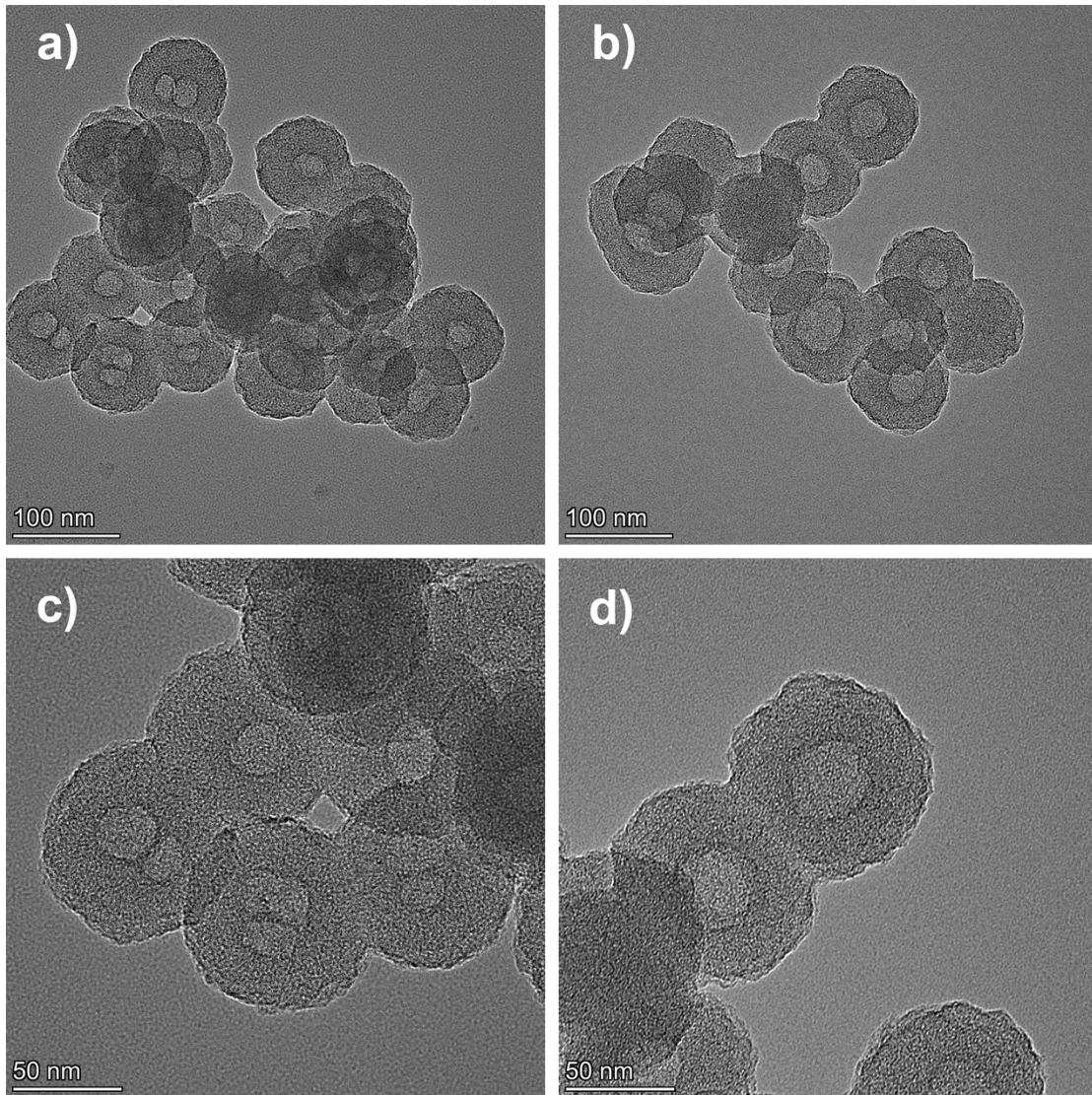
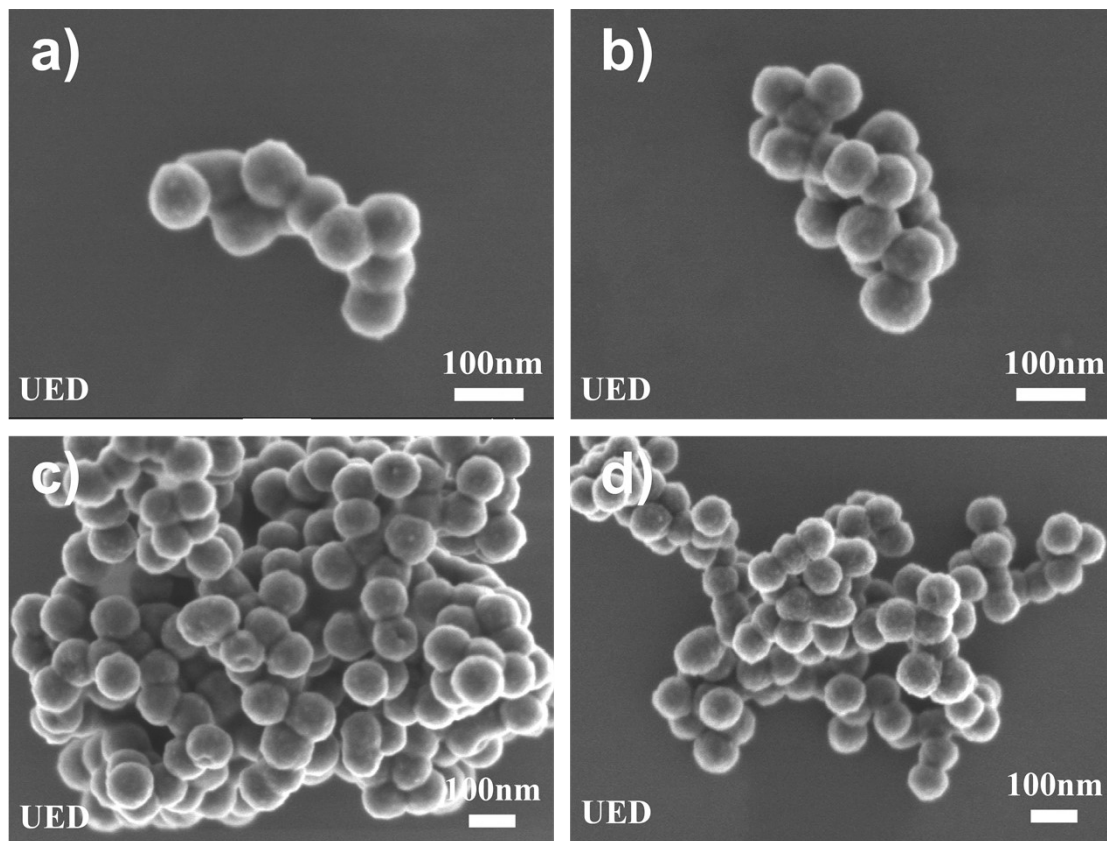**Fig. S4. a) b) c) and d) TEM images of HCNs-5h at different magnifications and regions.**

Fig. S5. High-resolution SEM images of HCNs and HCNs-5h: a) and c): HCNs, b) and d): HCNs-5h.
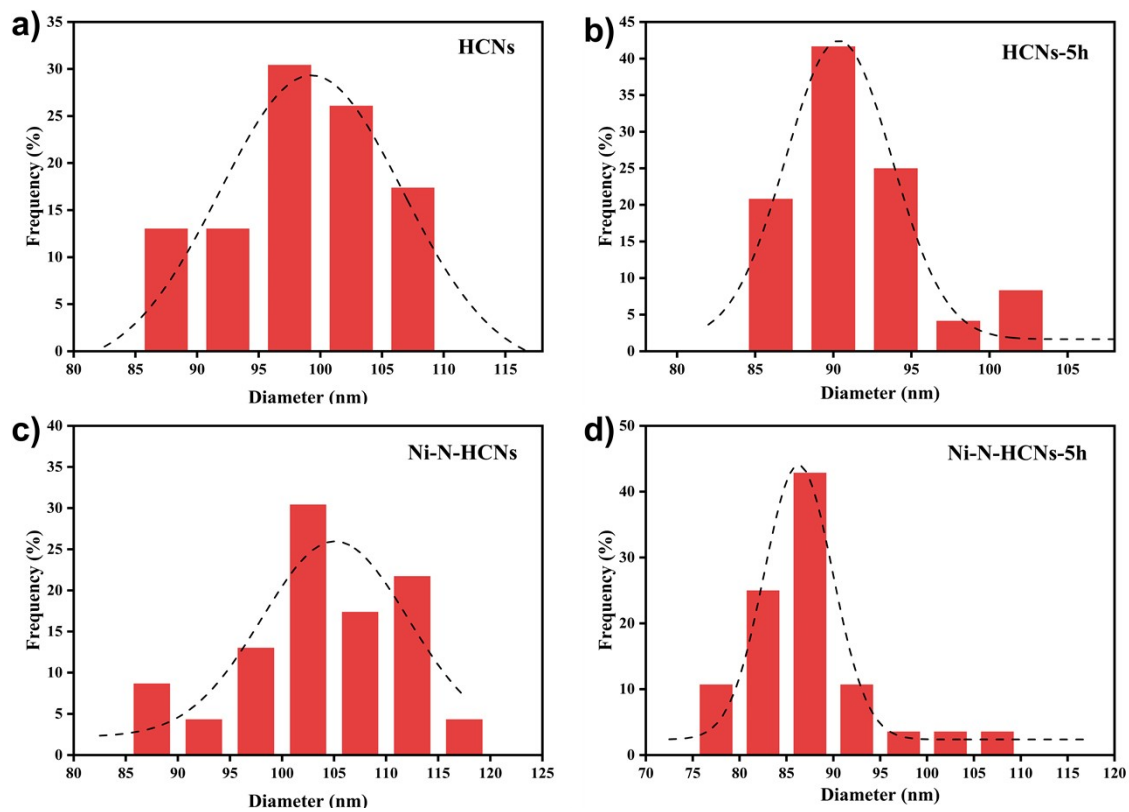
Fig. S6. Histogram of particle size frequency distribution based on TEM images: a) HCNs, b) HCNs-5h, c) Ni-N-HCNs, d) Ni-N-HCNs-5h.
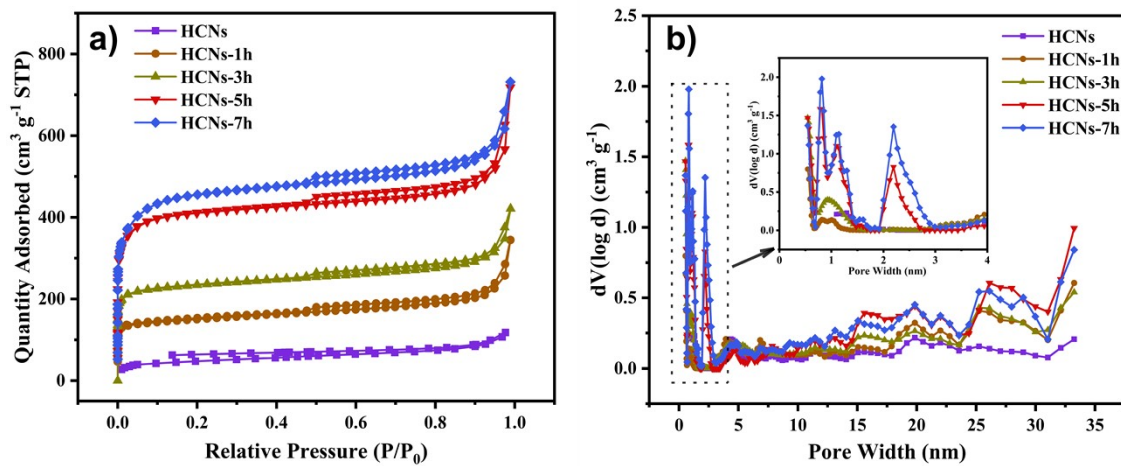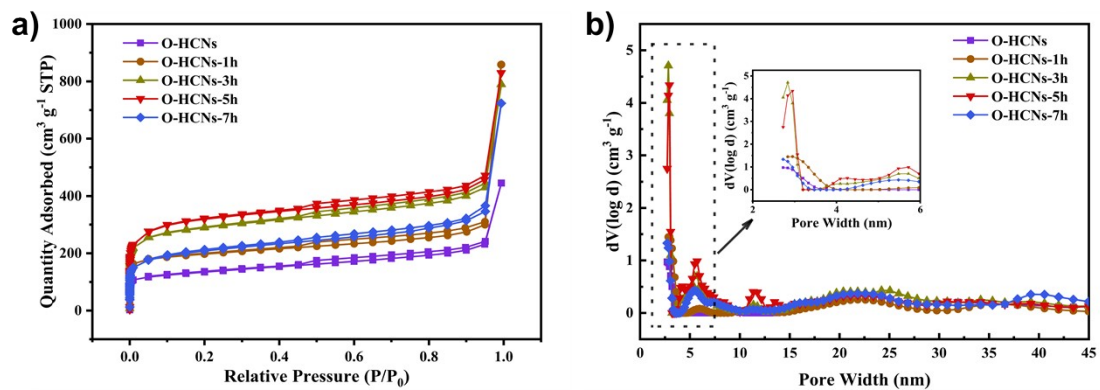
Fig. S7. a) Nitrogen adsorption-desorption isotherms and b) DFT pore size distribution of HCNs and HCNs-xh (the inset area shows the DFT pore size distribution, smaller than 5 nm).
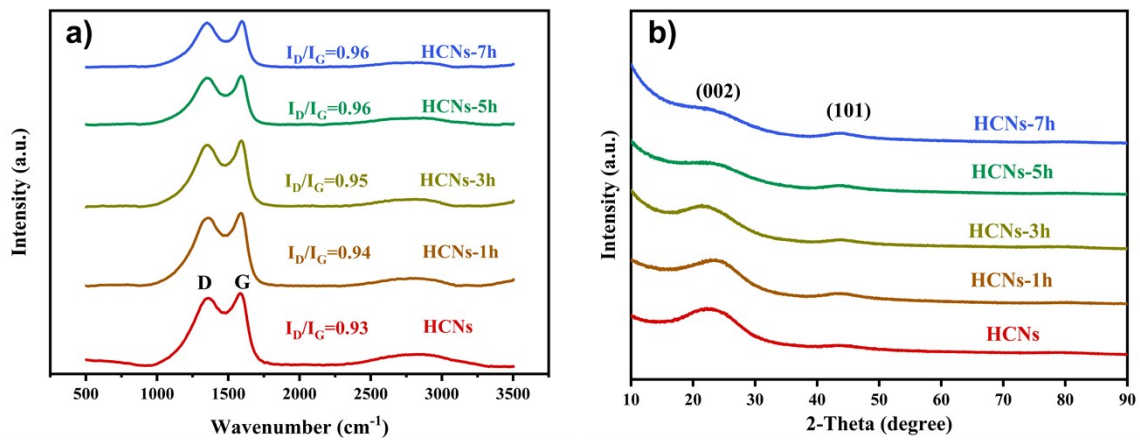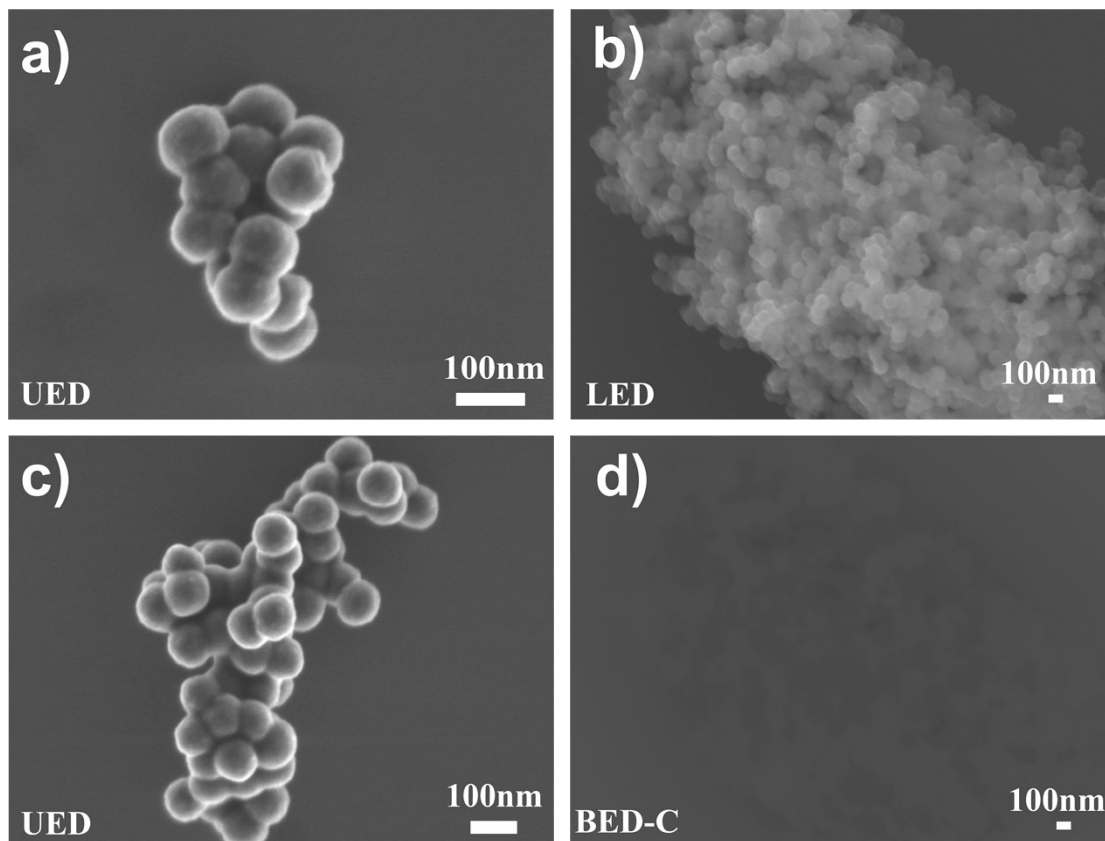
Fig. S8. a) Raman spectroscopy and b) XRD of HCNs and HCNs-xh.

Fig. S9. a) Nitrogen adsorption-desorption isotherms and **b)** DFT pore size distribution of O-HCNs and O-HCNs-xh (the inset area shows the DFT pore size distribution, which is smaller than 6 nm).

Fig. S10. a) and c) High-resolution SEM images of Ni-N-HCNs; b) Low-resolution SEM images and d) Backscatter images of Ni-N-HCNs.
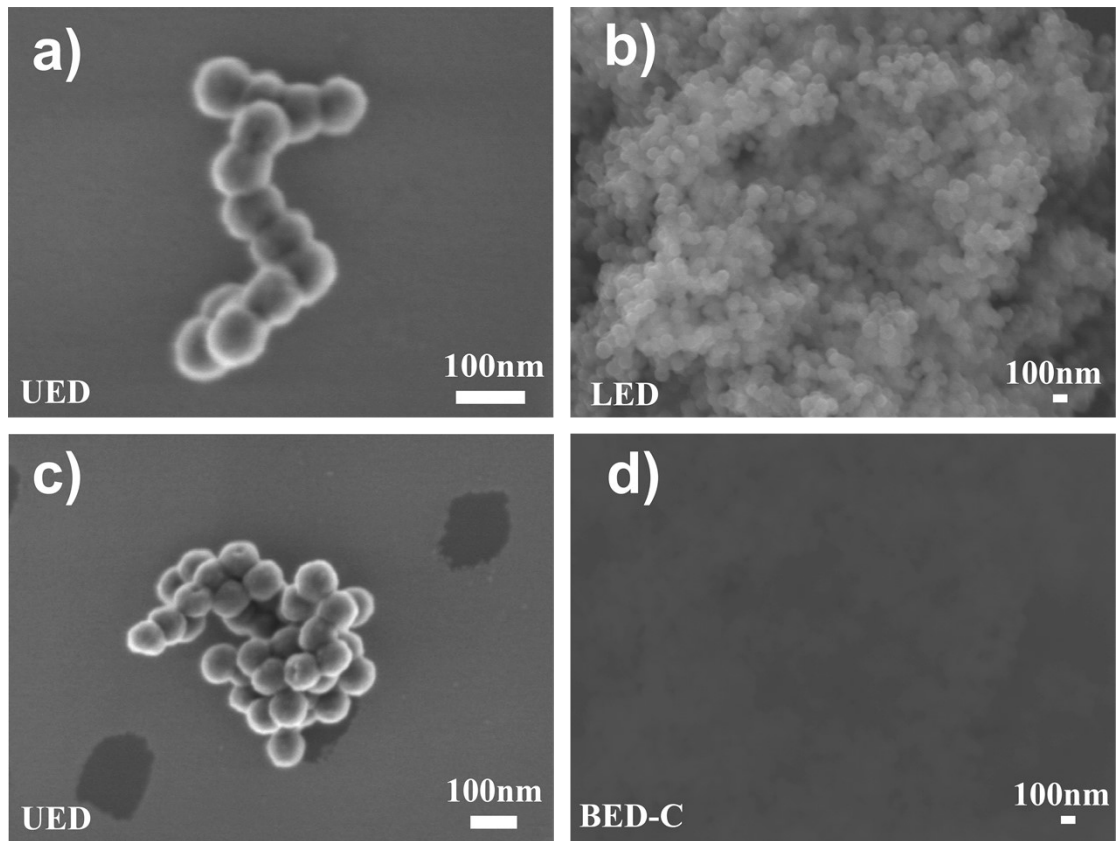
a) and c) High-resolution SEM images of Ni-N-HCNs-5h; b) Low-resolution SEM images and d) Backscatter images of Ni-N-HCNs-5h.

Fig. S11. a) and c) High-resolution SEM images of Ni-N-HCNs-5h; b) Low-resolution SEM images and d) Backscatter images of Ni-N-HCNs-5h.
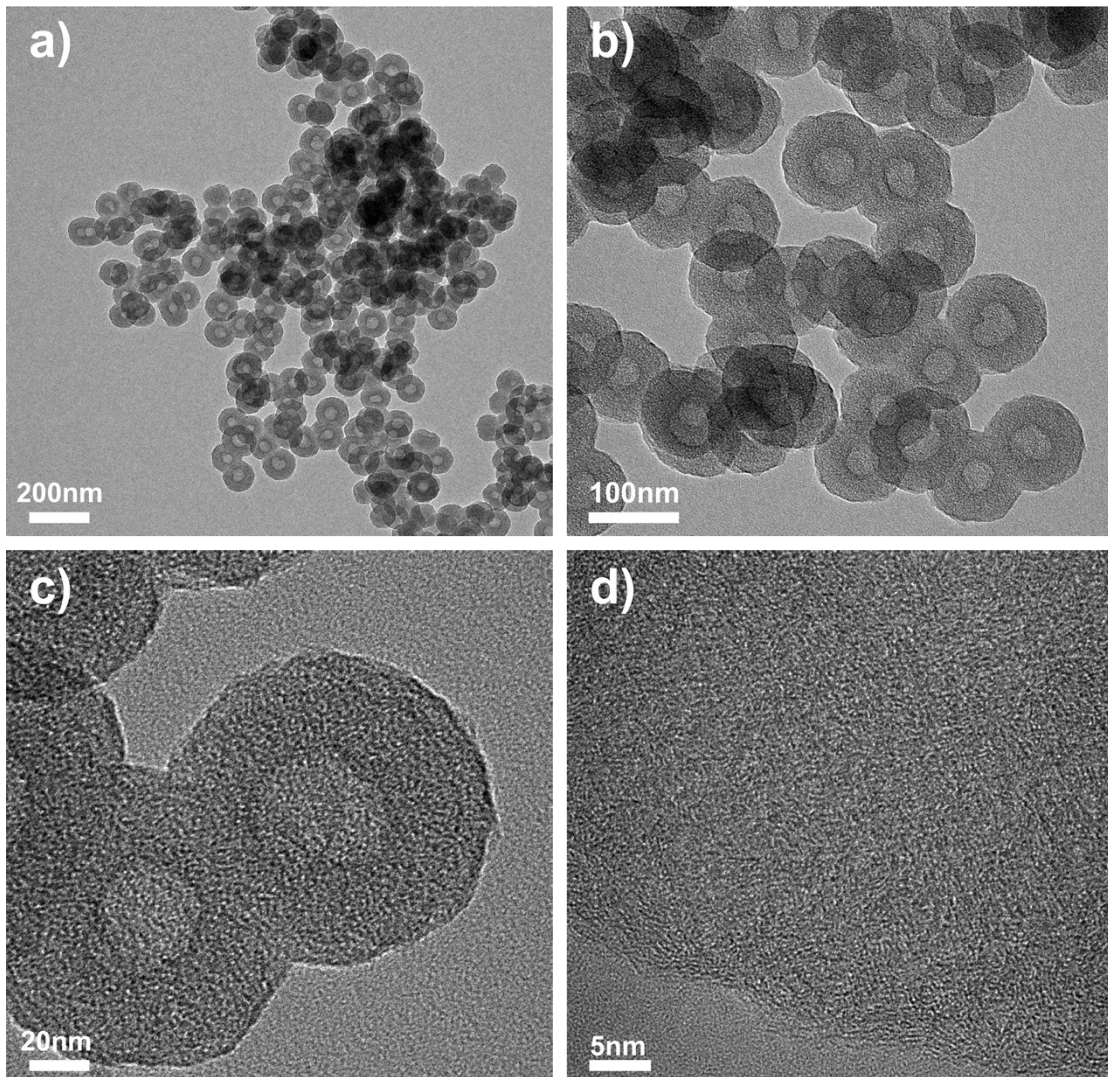
Fig. S12. a) and b) Low-resolution TEM images of Ni-N-HCNs; c) and d) high-resolution TEM images of Ni-N-HCNs.
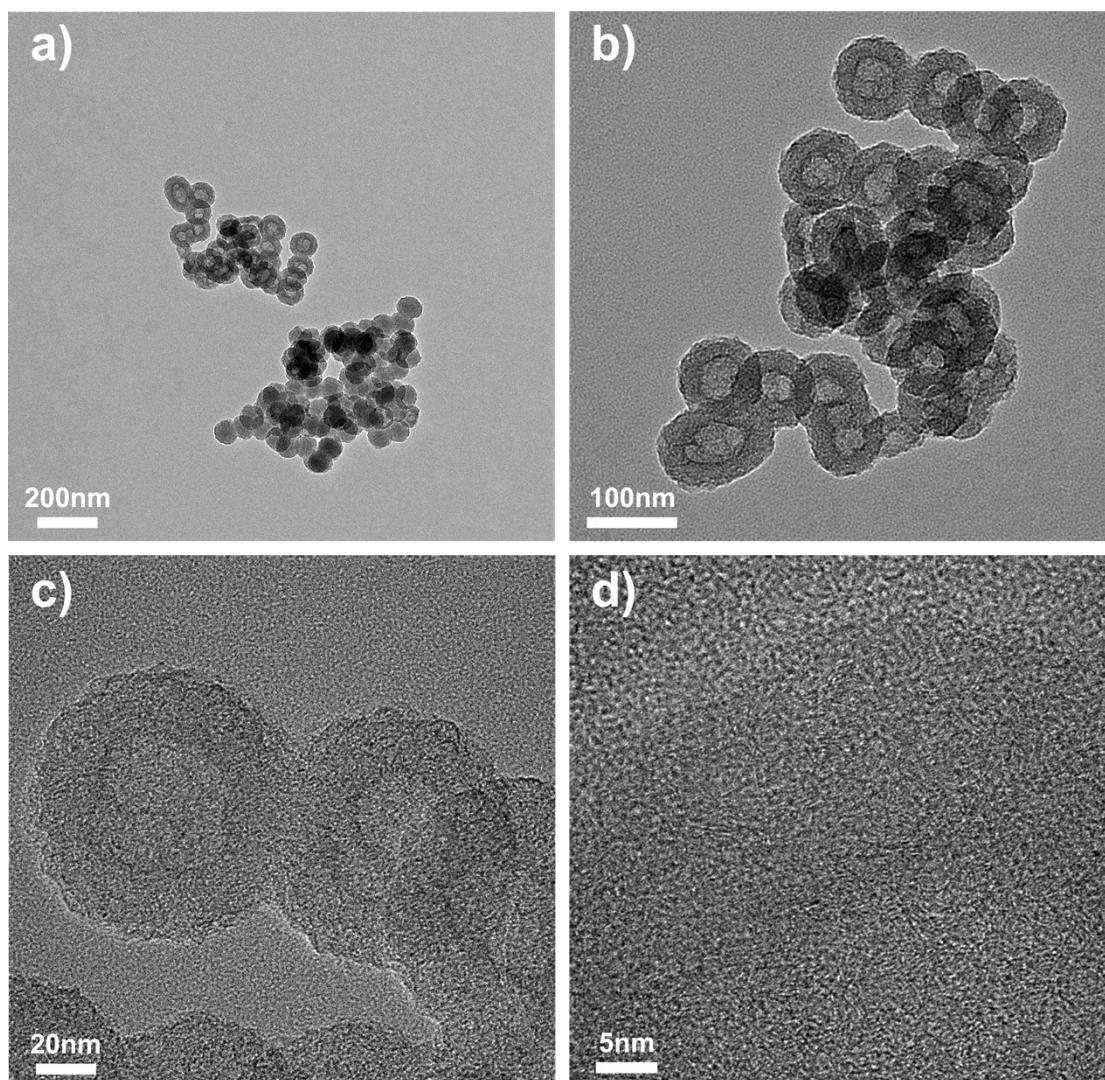
Fig. S13. a) and b) Low-resolution TEM images of Ni-N-HCNs-5h; c) and d) high-resolution TEM images of Ni-N-HCNs-5h.
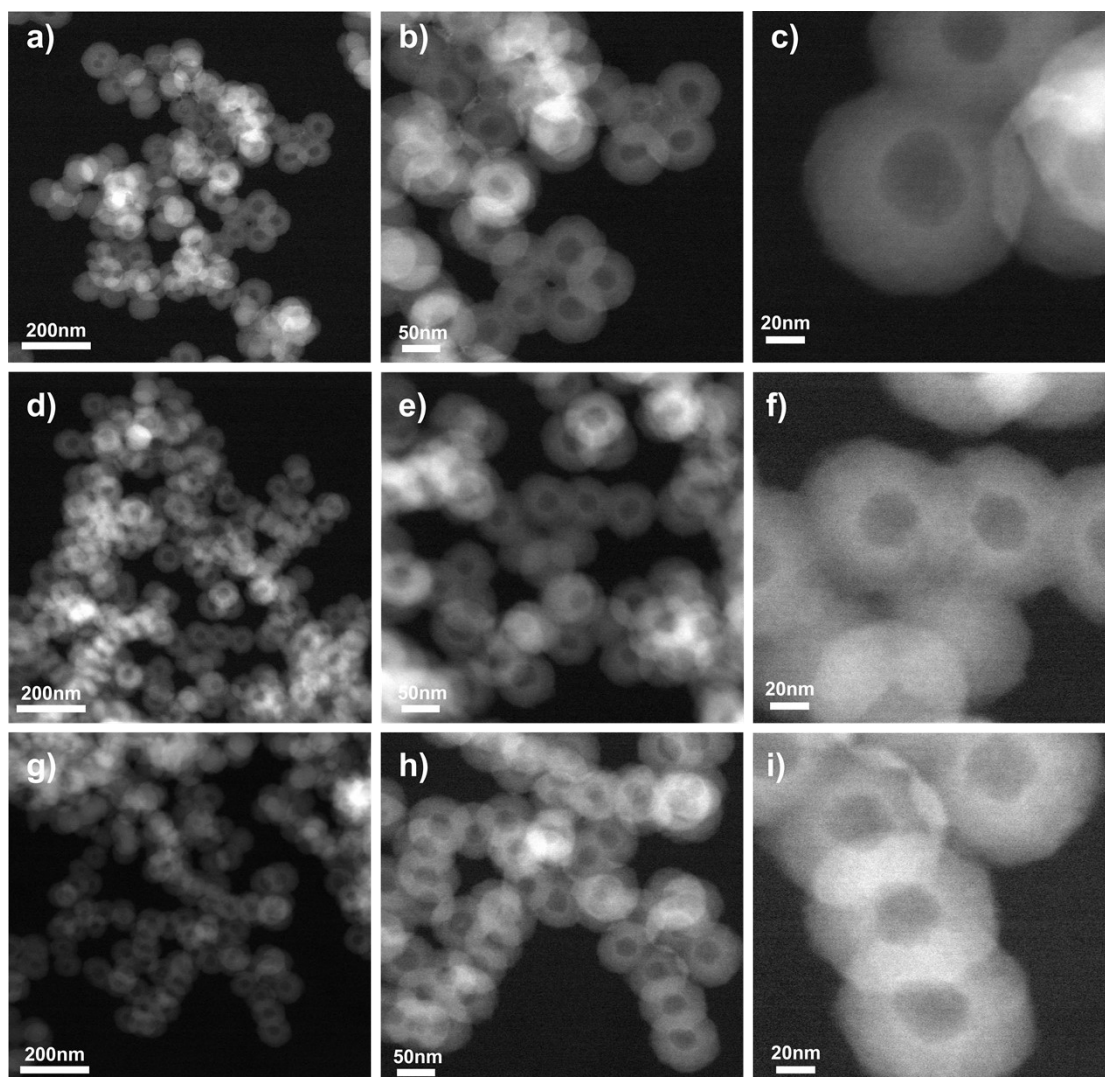
Fig. S14. a), b), and c) Low-resolution HAADF-STEM images of Ni-N-HCNs; d), e), and f) low-resolution HAADF-STEM images of Ni-N-HCNs-5h; g), h), and i) low-resolution HAADF-STEM images of Ni-N-HCNs-7h.
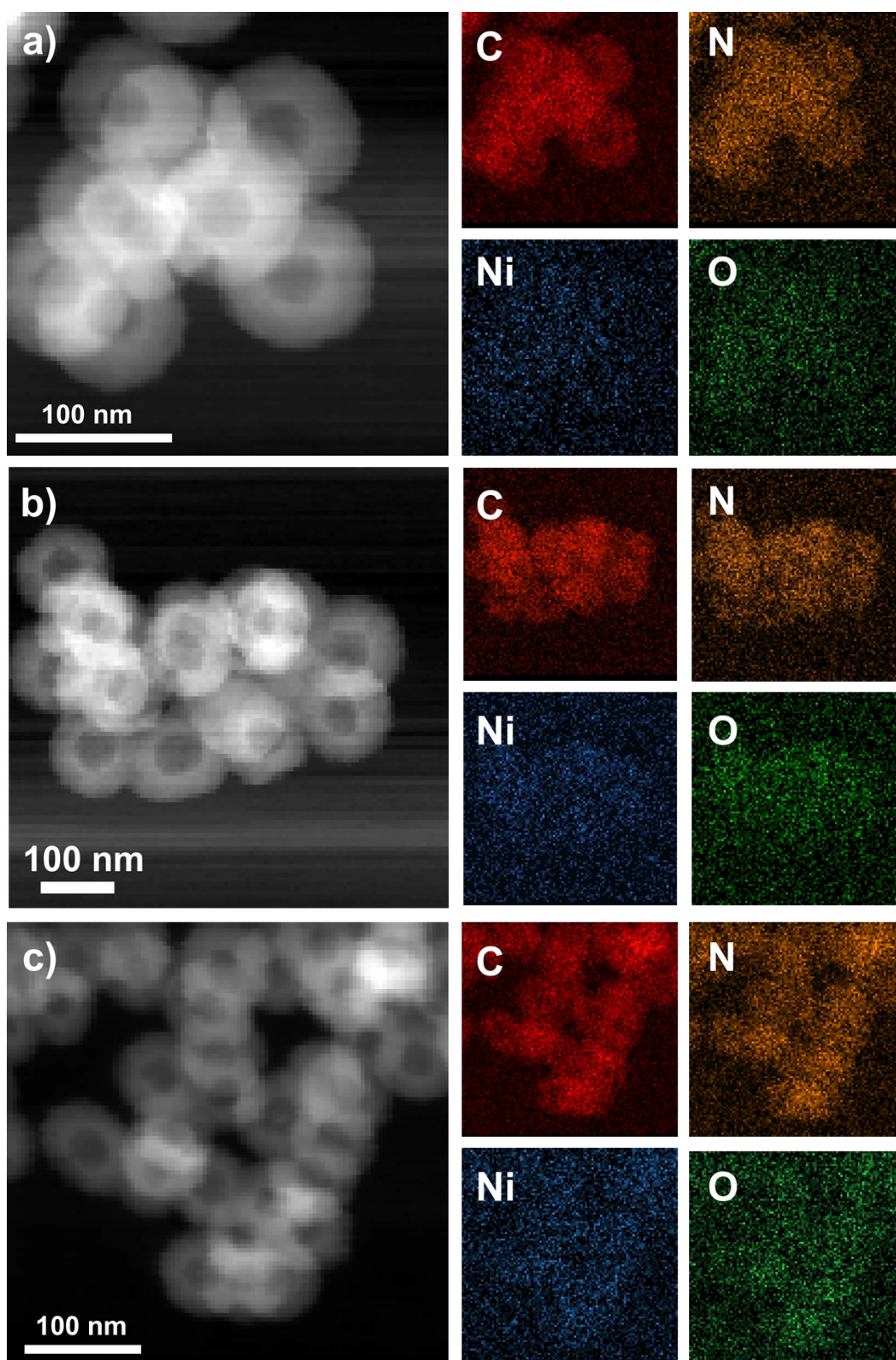
Fig. S15. a) Corresponding EDS images of low-resolution HAADF-STEM for C, N, Ni, and O in Ni-N-HCNs; b) corresponding EDS images of low-resolution HAADF-STEM for C, N, Ni, and O in Ni-N-HCNs-5h; c) corresponding EDS images of low-resolution HAADF-STEM for C, N, Ni, and O in Ni-N-HCNs-7h
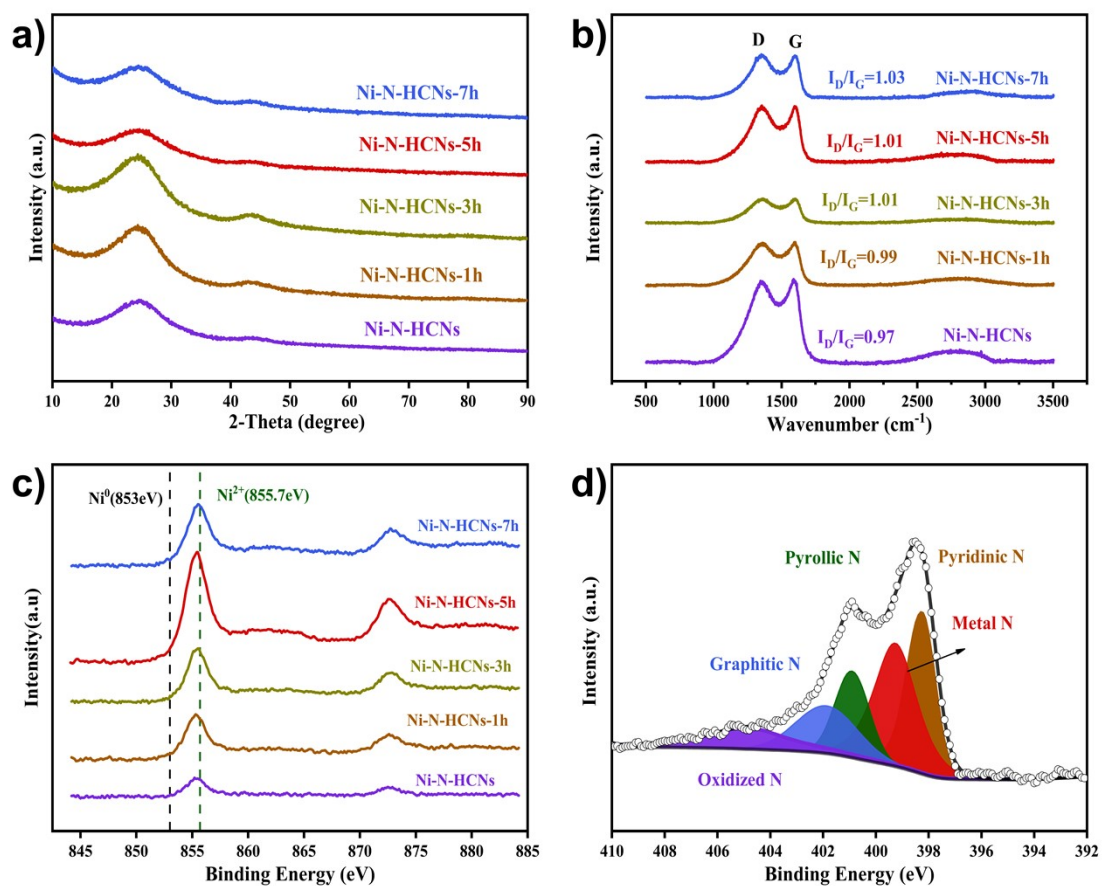
Fig. S16. a) XRD patterns of Ni-N-HCNs and Ni-N-HCNs-xh, b) Raman spectroscopy of Ni-N-HCNs-xh and Ni-N-HCNs, c) Ni 2p high-resolution XPS surveys of Ni-N-HCNs and Ni-N-HCNs-xh, d) N 1s high-resolution XPS spectra of Ni-N-HCNs-5h.
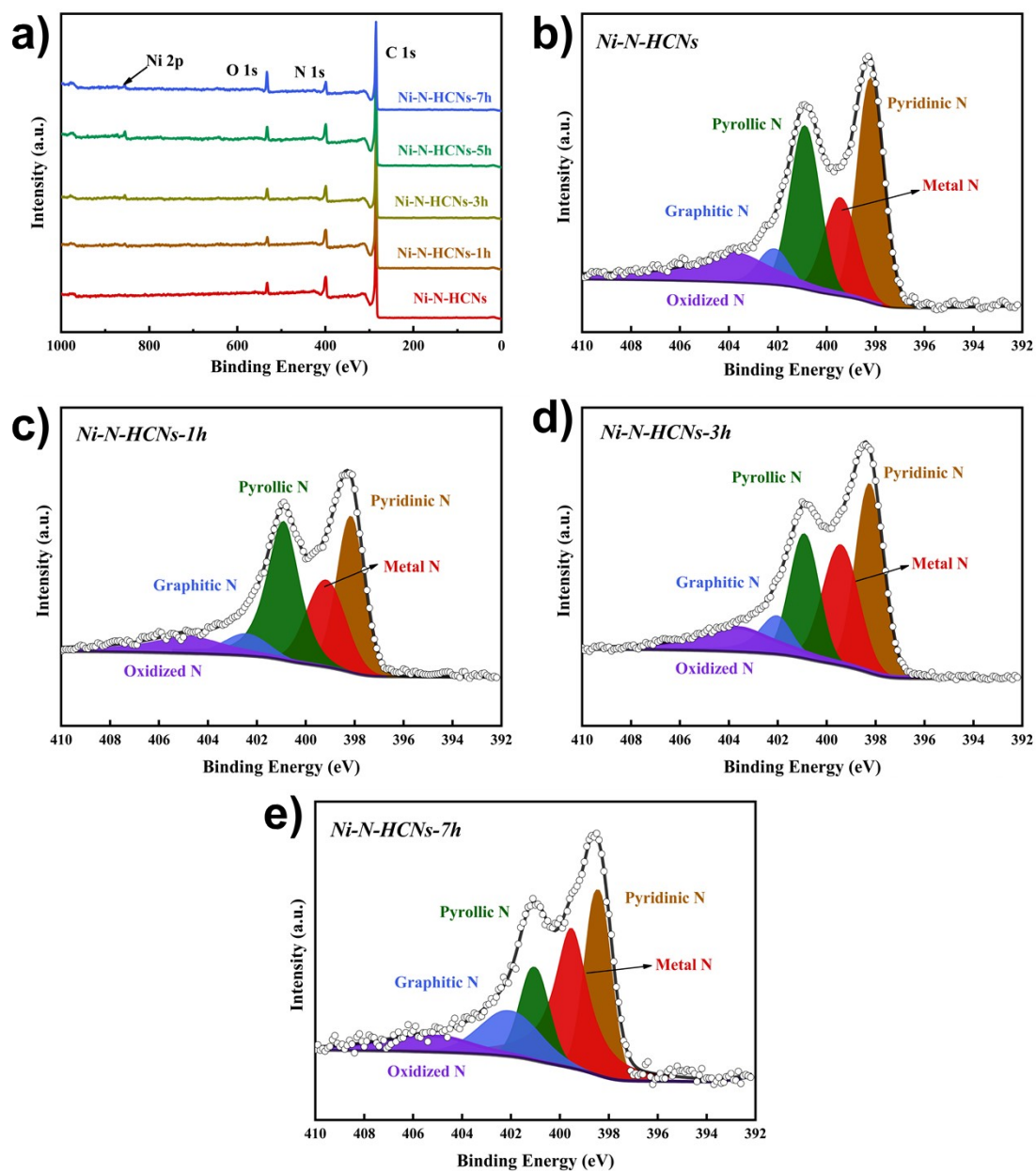
Fig. S17. a) XPS survey of Ni-N-HCNs and Ni-N-HCNs-xh; N 1s XPS spectra of Ni-N-HCNs-xh: b) Ni-N-HCNs, c) Ni-N-HCNs-1h, d) Ni-N-HCNs-3h, and e) Ni-N-HCNs-7h.
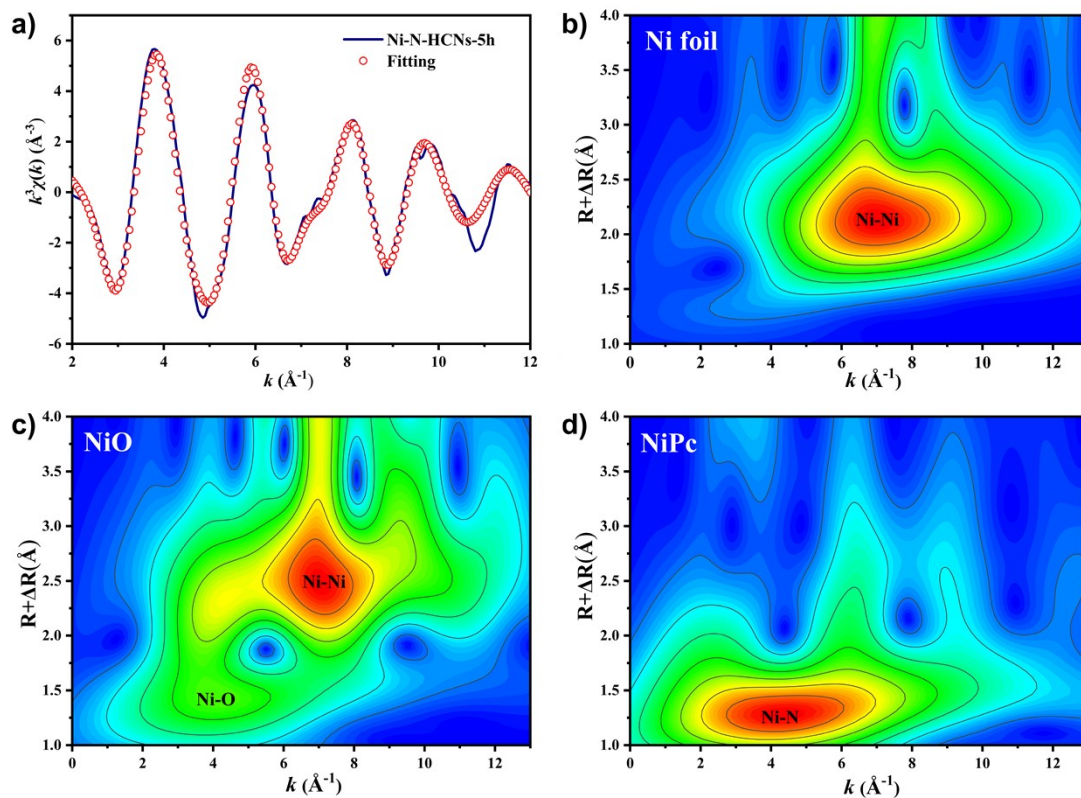
Fig. S18. a) The EXAFS fitting in K-space for Ni-N-HCNs-5h, WT spectra of different examples as reference: b) Ni foil, c) NiO, and d) NiPc.

Fig. S19. Applied potential dependence of total current density over a) Ni-N-HCNs, b) Ni-N-HCNs-1h, c) Ni-N-HCNs-3h, d) Ni-N-HCNs-5h and e) Ni-N-HCNs-7h in CO_2-saturated 0.5 M $KHCO_3$ solution with a catalyst loading of 1.5 ± 0.1 mg cm^{-2} for all catalysts.
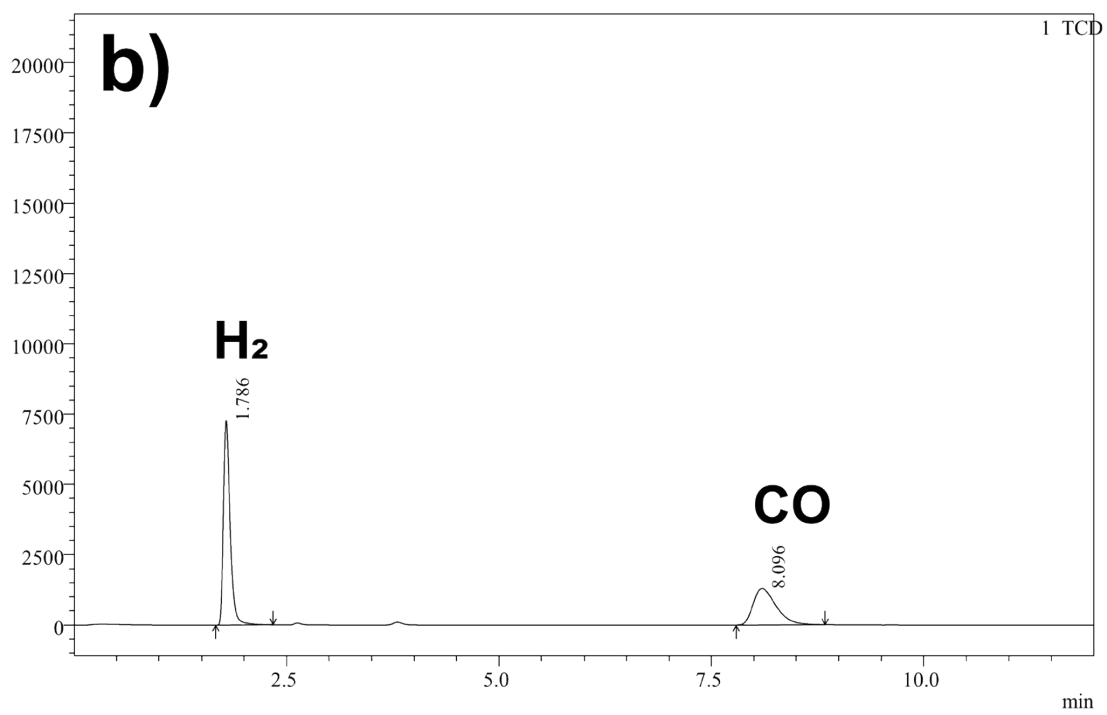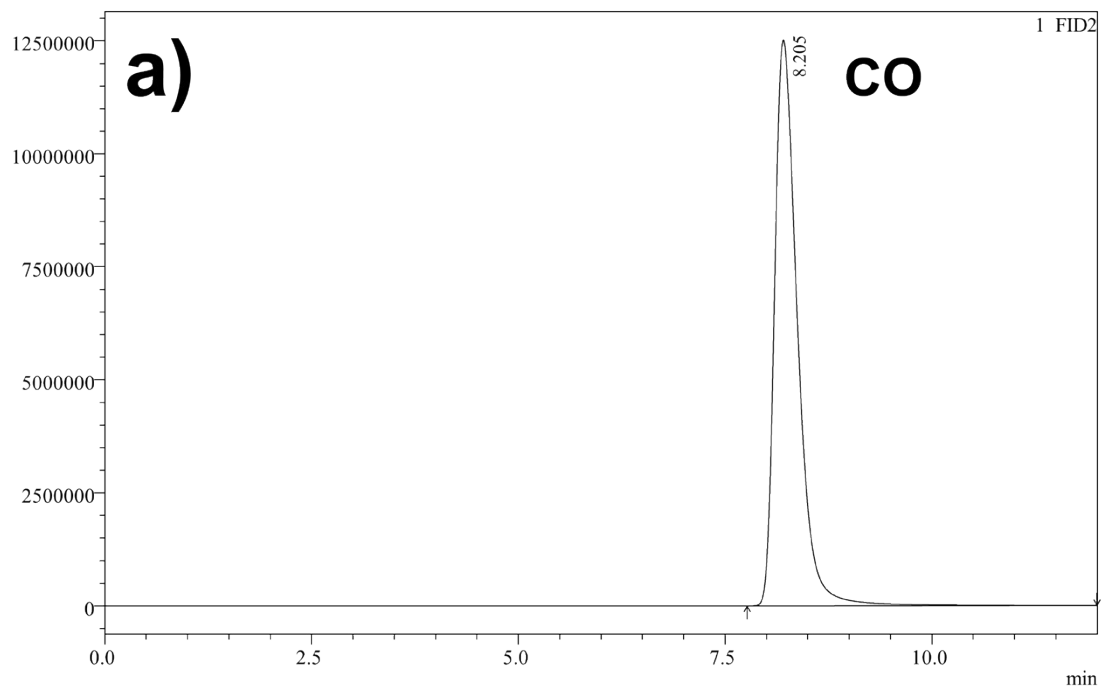
Fig. S20. Gas product detection by Shimazu GC-2014C for Ni-N-HCNs-5h at -1.0V/RHE.

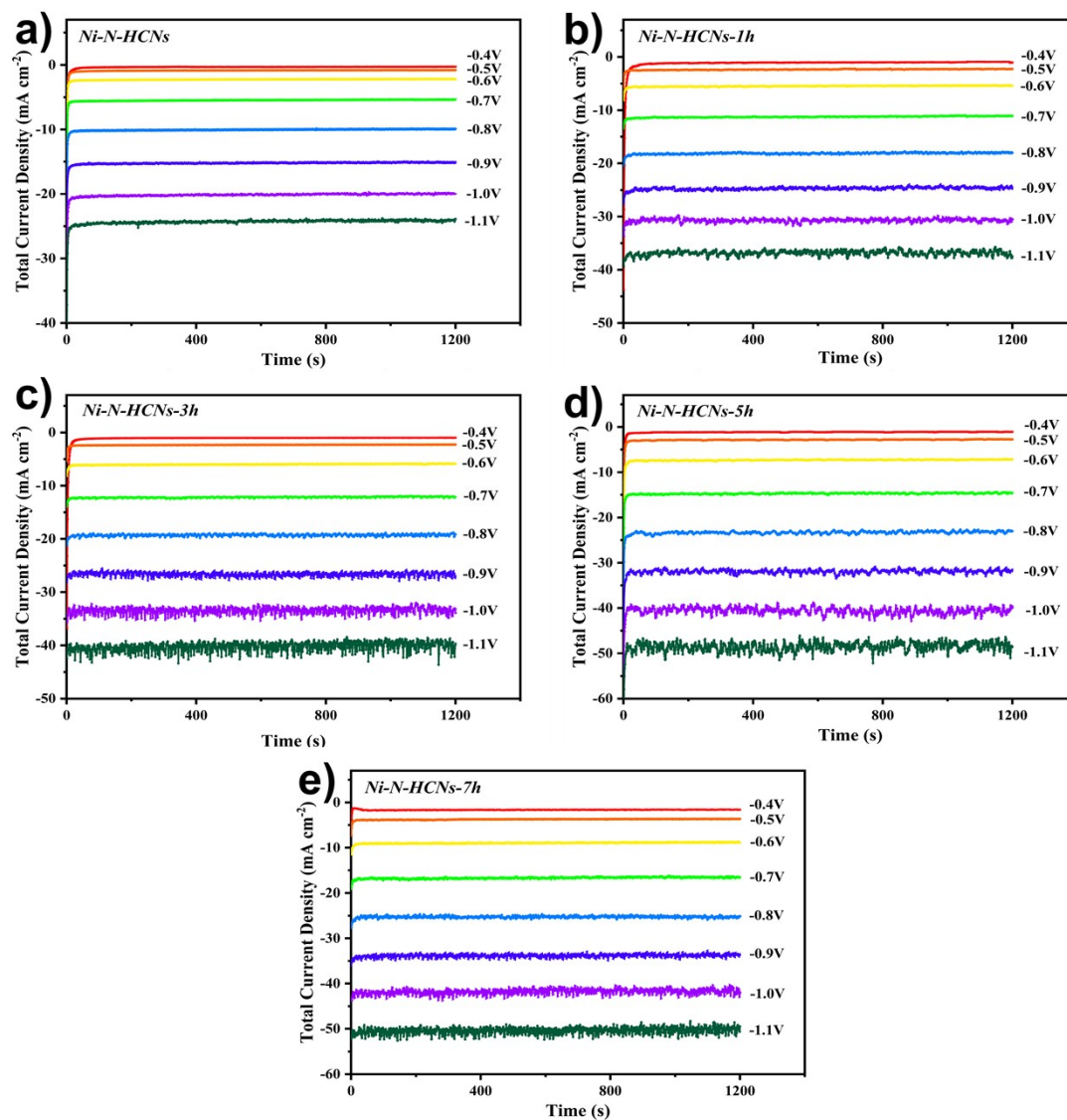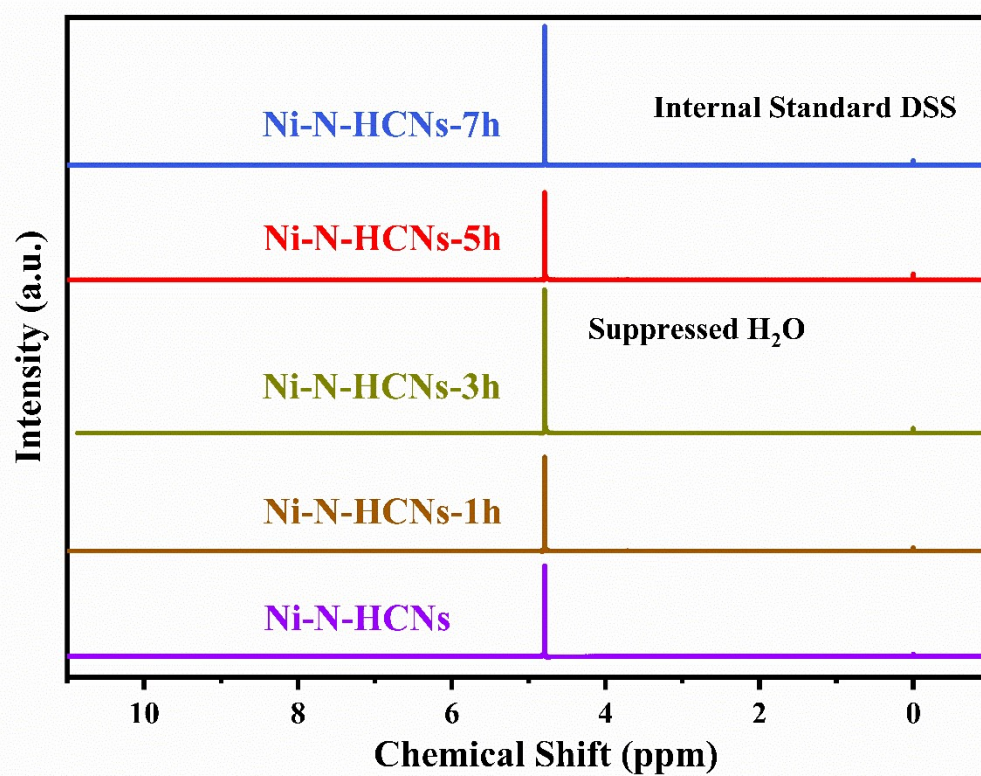Fig. S21. Liquid product detection by NMR for Ni-N-HCNs and Ni-N-HCNs-xh.
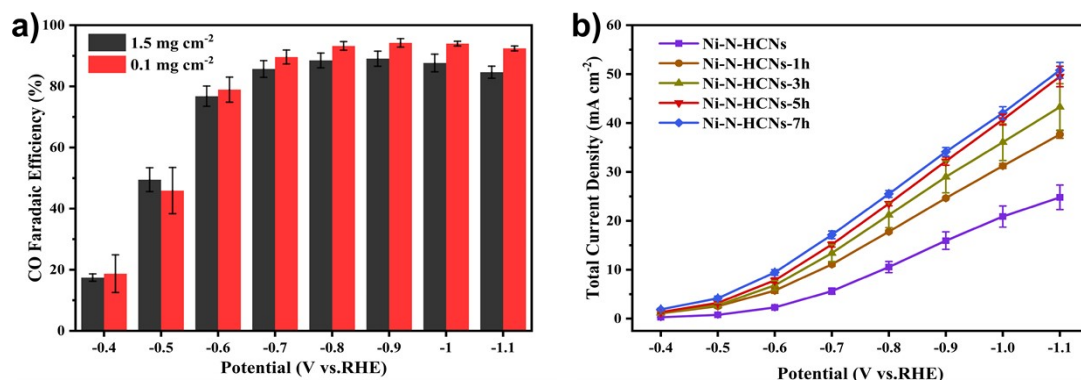
Fig. S22. a) CO Faradaic Efficiency for Ni-N-HCNs-5h with a catalyst loading of 0.1 mg cm^{-2} and 1.5 mg cm^{-2}, **b)** Total current density of Ni-N-HCNs and Ni-N-HCNs-xh under different applied potential measured in CO_2-saturated 0.5 M $KHCO_3$ solution.

Fig. S23. Contact angle measurement of working electrode with Ni-N-HCNs-5h before and after stability test: a) original, b) after durability test, after durability test and standing c) 5 s, d) 10s, e) 15s, and f) 20s.
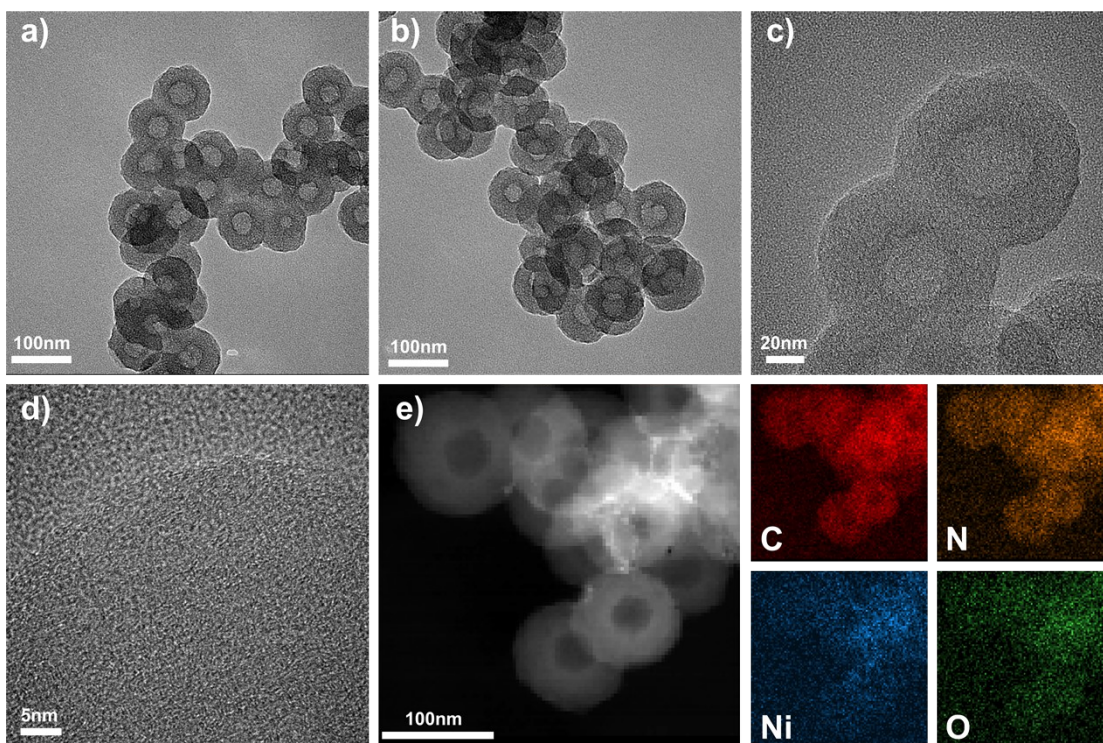
Fig. S24. HRTEM images of Ni-N-HCNs-5h after 50 h stability test: a), b), c), and d); low-resolution HAADF-STEM images and the corresponding EDS images for C, N, Ni, and O of Ni-N-HCNs-5h.
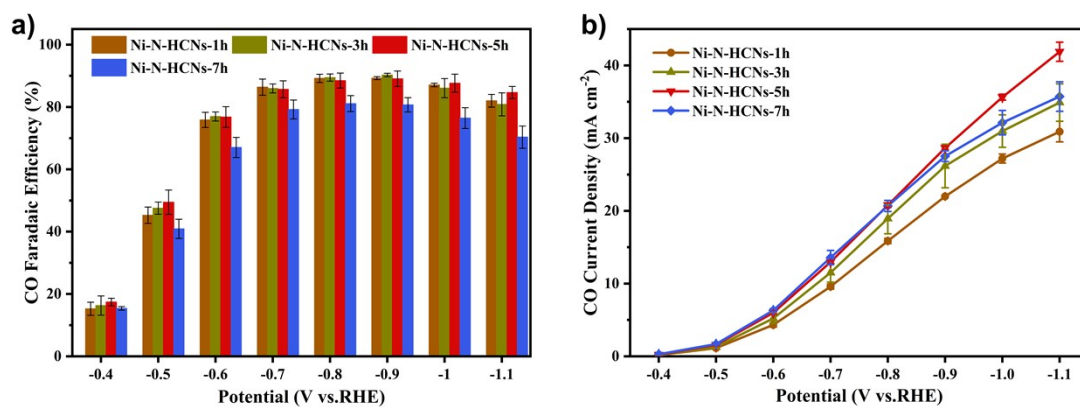
Fig. S25. a) CO Faradaic Efficiency and b) CO partial current density of Ni-N-HCNs-xh catalyst under different applied potentials measured in CO2-saturated 0.5 M KHCO$_3$ solution with a catalyst loading of 1.5 ± 0.1 mg cm^{-2}.
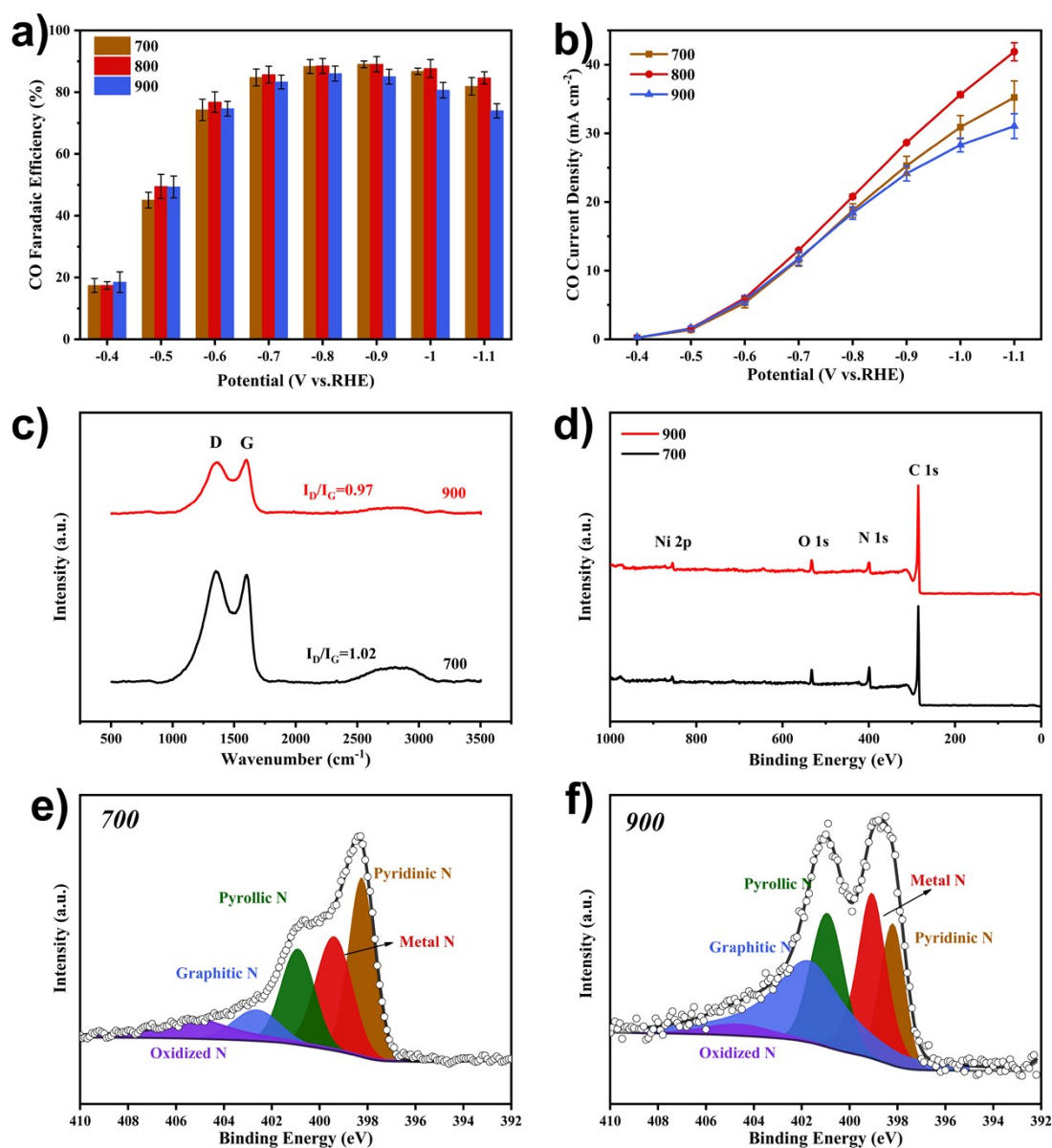
Fig. S26. a) CO Faradaic Efficiency and b) CO partial current density of Ni-N-HCNs-5h prepared at different pyrolysis temperatures under different applied potentials measured in CO2-saturated 0.5 M KHCO$_3$ solution with a catalyst loading of 1.5 ± 0.1 mg cm^{-2}, c) Raman spectra and d) XPS survey of Ni-N-HCNs-5h prepared at different pyrolysis temperature, e) and f) N1 XPS spectra of Ni-N-HCNs-5h prepared at different pyrolysis temperature.
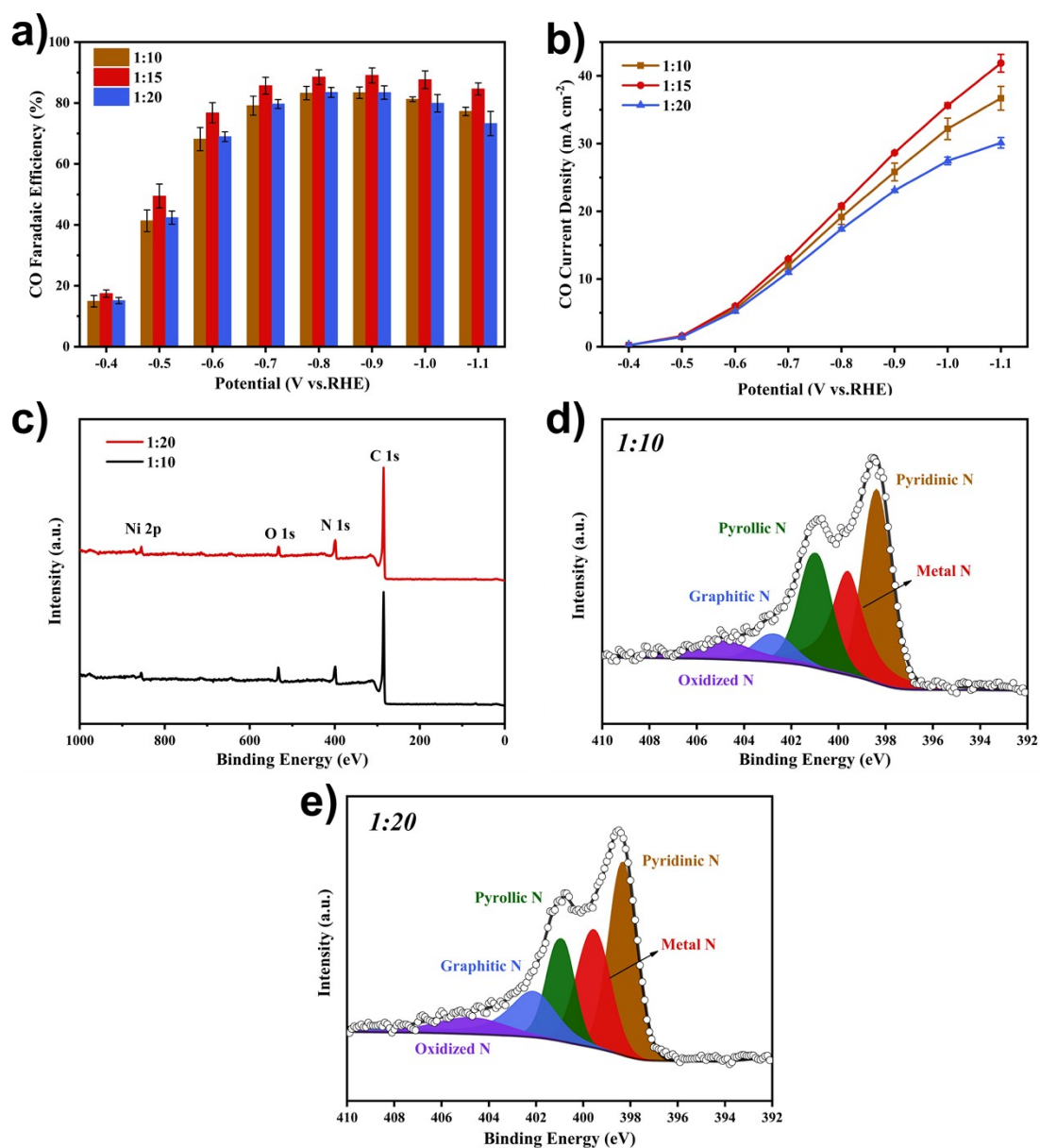
Fig. S27. a) CO Faradaic Efficiency and b) CO partial current density of Ni-N-HCNs-5h prepared by different doping content of C_3N_4 under different applied potentials measured in CO_2-saturated 0.5 M $KHCO_3$ solution with a catalyst loading of 1.5 ± 0.1 mg cm^{-2}, c) XPS survey of Ni-N-HCNs-5h prepared by different doping content of C_3N_4, e) and f) N1 XPS spectra of Ni-N-HCNs-5h prepared by different doping content of C_3N_4.

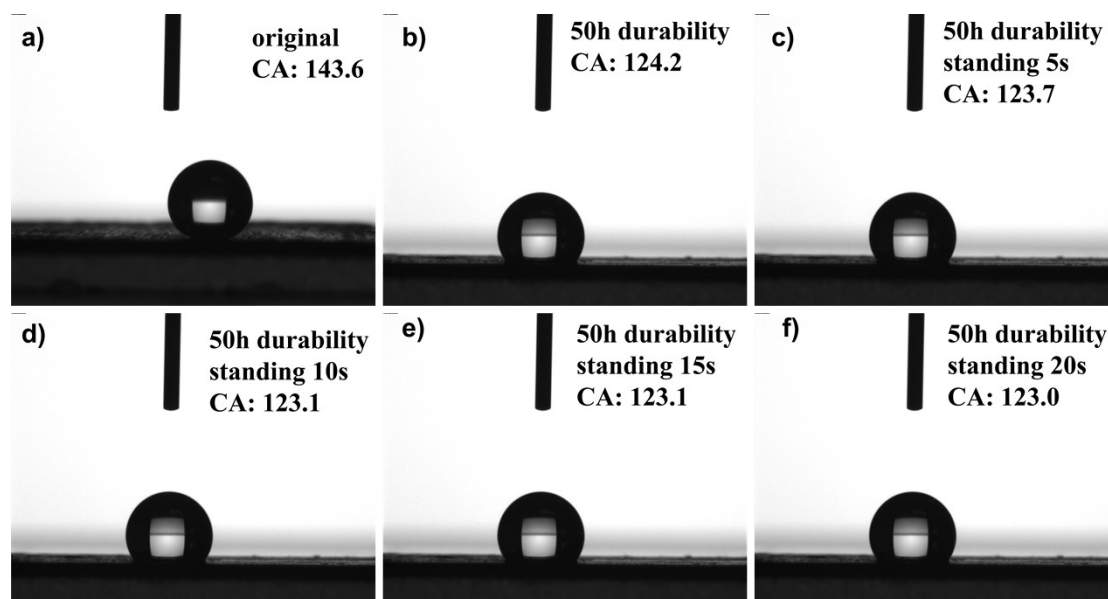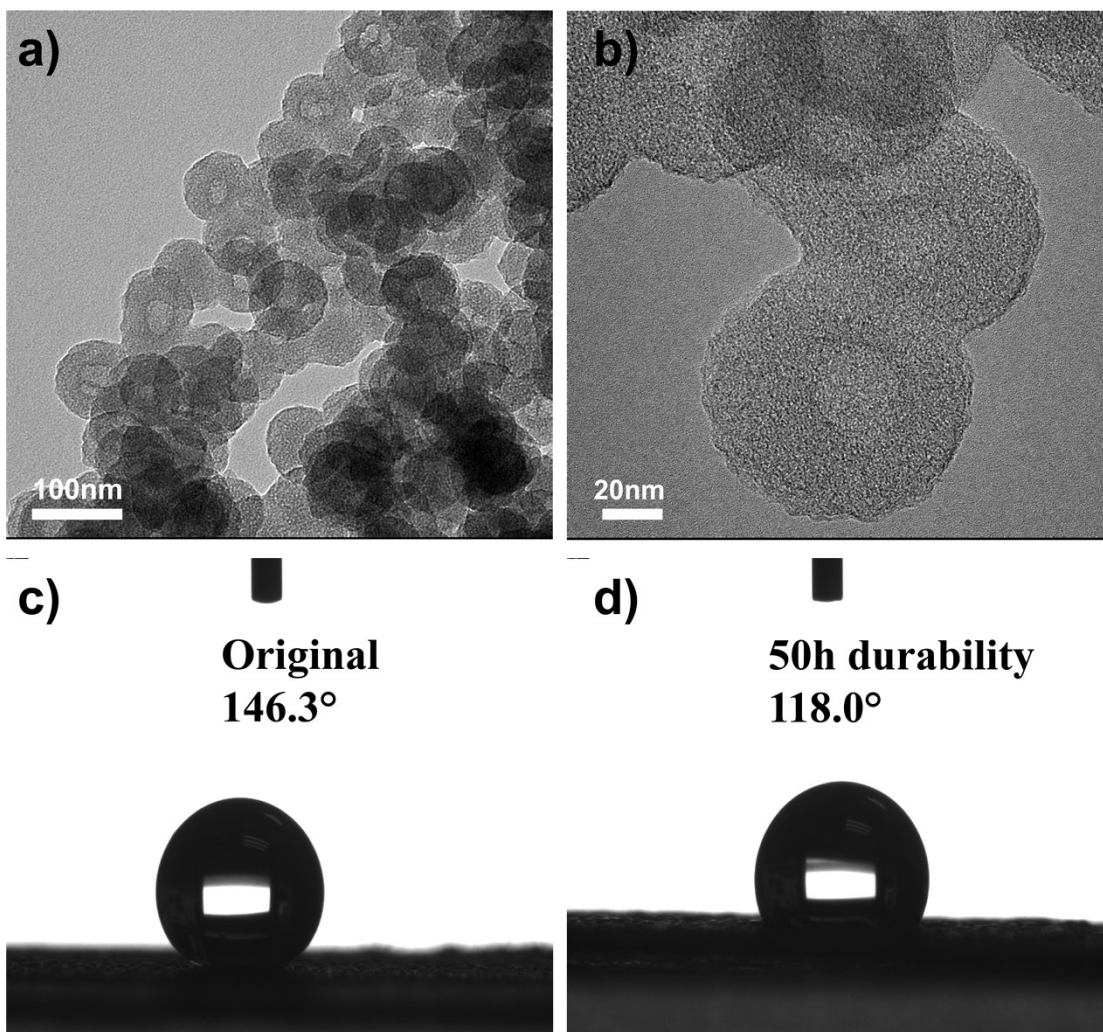**Fig. S28.** a) and b) High-resolution TEM images of Ni-N-HCNs-5h after stability test, contact angle measurement of working electrode with Ni-N-HCNs-5h before and after stability test in flow cell: a) original, b) after durability.
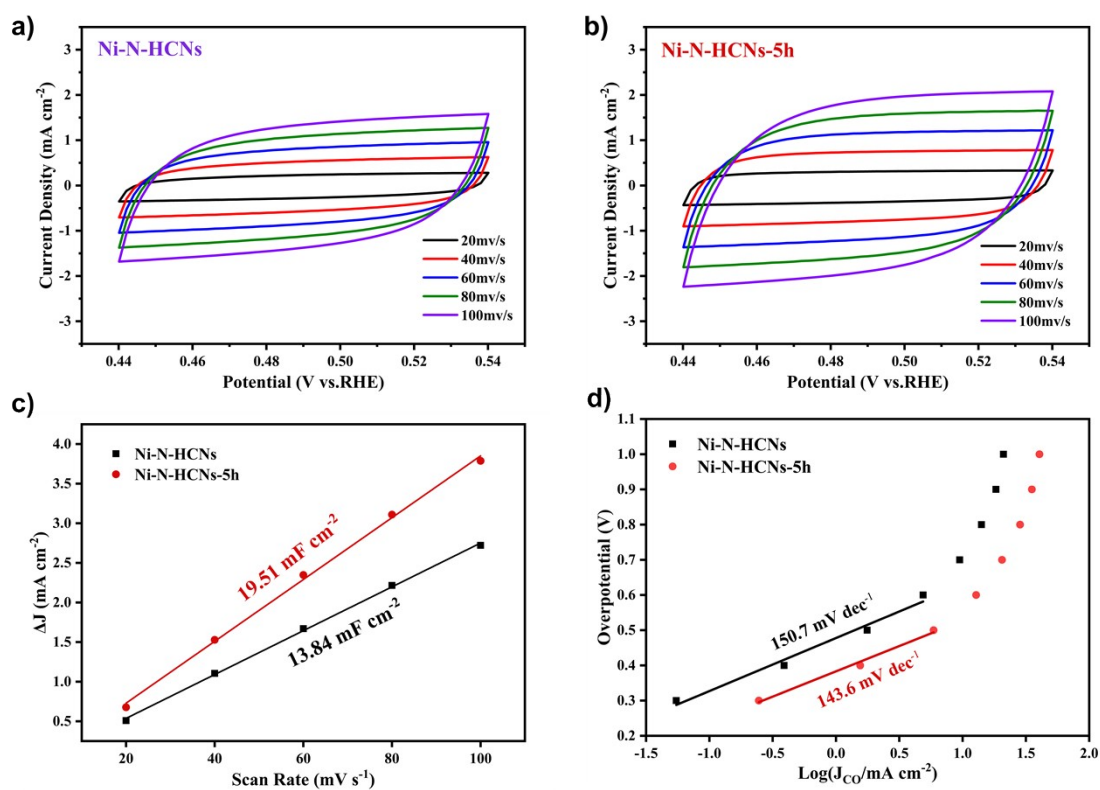
Fig. S29. CV curves at the range of 0.44 to 0.54V vs. RHE with different scan rates (20, 40, 60, 80, and 100 mV/s) for a) Ni-N-HCNs, and b) Ni-N-HCNs-5h. c) Linear fitting of double-layer capacitive currents ΔJ at 0.49 V vs. RHE against scan rates in N_2-saturated 0.5 M $KHCO_3$ solution for Ni-N-HCNs and Ni-N-HCNs-5h. d) Tafel plots of CO production for Ni-N-HCNs and Ni-N-HCNs-5h.
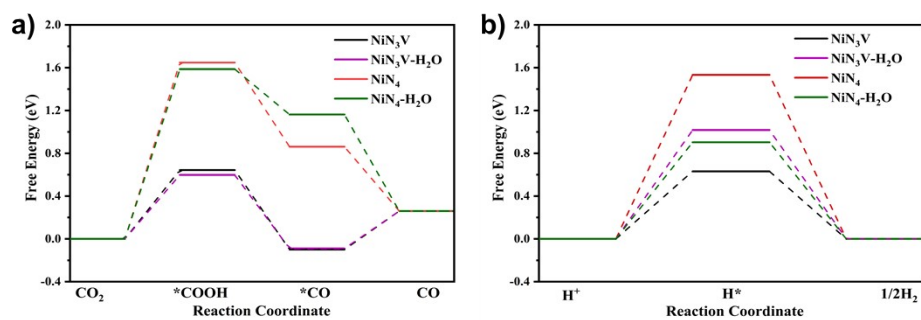
Fig. S30. a) Calculated free energy diagram for ECR to CO on NiN$_4$ and NiN$_3$V sites in the presence and absence of H$_2$O molecules, b) Calculated free energy diagram for HER on NiN$_4$ and NiN$_3$V sites in the presence and absence of H$_2$O molecules.

Table S1. As obtained CO and H_2 Faradaic efficiencies in comparison with the CO Faradaic efficiencies after the normalization process on Ni-N-HCNs, Ni-N-HCNs-5h and Ni-N-HCNs-7h

Ni-N-HCNs	-0.6V	-0.7V	-0.8V	-0.9V
Normalized CO FE/%	87.8	94.0	96.2	95.9
As obtained CO FE/%	90.3	100.8	105.1	100.7
As obtained H_2 FE/%	12.5	6.4	4.1	4.3
As obtained (CO+H_2) FE/%	102.8	107.2	109.2	105.0

Test condition: Measured in CO2-saturated 0.5 M $KHCO_3$ solution with a catalyst loading of 1.5 ± 0.1 mg cm^{-2}

Ni-N-HCNs-5h	-0.6V	-0.7V	-0.8V	-0.9V
Normalized CO FE/%	74.3	84.1	87.5	89.1
As obtained CO FE/%	82.4	90.4	99.4	100.4
As obtained H_2 FE/%	28.5	17.0	14.2	12.2
As obtained (CO+H_2) FE/%	110.9	107.4	113.6	112.7

Test condition: Measured in CO2-saturated 0.5 M $KHCO_3$ solution with a catalyst loading of 1.5 ± 0.1 mg cm^{-2}

Ni-N-HCNs-7h	-0.6V	-0.7V	-0.8V	-0.9V
Normalized CO FE/%	65.7	81.6	79.8	79.1
As obtained CO FE/%	70.6	82.8	88.4	87.7
As obtained H_2 FE/%	36.9	18.7	22.5	23.2
As obtained (CO+H_2) FE/%	107.5	101.6	110.9	110.9

Test condition: Measured in CO2-saturated 0.5 M $KHCO_3$ solution with a catalyst loading of 1.5 ± 0.1 mg cm^{-2}

Table S2. BET surface areas and pore distribution of HCNs and HCNs-xh based on the N$_2$ adsorption-desorption isotherms

Sample	BET surface area (m^2 g^{-1})	Micropore surface area (m^2 g^{-1})	Total pore volume (cm^3 g^{-1})	Micropore pore volume (cm^3 g^{-1})	Yield (%)
HCNs	177.2	81.6	0.18	0.03	43
HCNs-1h	572.1	439.7	0.53	0.18	35
HCNs-3h	906.6	768.2	0.65	0.30	28
HCNs-5h	1591.0	1443.6	1.11	0.57	21
HCNs-7h	1726.5	1541.7	1.13	0.63	18

Note: $yield = M(HCNs - xh)/M(PACP) \times 100\%$ where; M(HCNs-xh) refers to the mass of HCNs-xh and HCNs, g; M(PACP) refers to the mass of PACP, g.

Table S3. BET surface areas and pore distribution of Ni-N-HCNs and Ni-N-HCNs-xh based on the N$_2$ adsorption-desorption isotherms

Example	BET surface area (m$_2$ g^{-1})	Micropore surface area (m^2 g^{-1})	Total pore volume (cm^3 g^{-1})	Mesopore volume (cm^3 g^{-1})
Ni-N-HCNs	489.0	199.2	0.55	0.46
Ni-N-HCNs-1h	695.1	456.2	0.61	0.41
Ni-N-HCNs-3h	977.6	654.5	0.85	0.57
Ni-N-HCNs-5h	1104.8	791.7	1.07	0.67
Ni-N-HCNs-7h	1103.7	650.8	1.06	0.73

Table S4. The content of various elements content quantified by XPS, and Ni content quantified by ICP-OES for Ni-N-HCNs and Ni-N-HCNs-xh.

Example	C (wt.%)	N (wt.%)	O (wt.%)	Ni (wt.%)	Ni (ICP) (wt.%)
Ni-N-HCNs	77.31	17.27	5.11	0.32	0.22
Ni-N-HCNs-1h	80.36	14.25	4.2	1.19	1.07
Ni-N-HCNs-3h	79.09	12.99	6.55	1.37	1.96
Ni-N-HCNs-5h	80.39	11.99	5.41	2.21	2.28
Ni-N-HCNs-7h	80.13	7.17	10.66	2.04	3.30

Table S5. The content of different configurations of nitrogen derived from N 1s XPS for Ni-N-HCNs and Ni-N-HCNs-xh.

Example	Pyridinic N (wt.%)	Metal N (wt.%)	Pyrrolic N (wt.%)	Graphitic N (wt.%)	Oxidized N (wt.%)
Ni-N-HCNs	5.61	3.04	4.59	1.18	2.87
Ni-N-HCNs-1h	3.92	3.07	4.86	0.88	1.52
Ni-N-HCNs-3h	4.04	3.29	2.79	1.13	1.74
Ni-N-HCNs-5h	3.18	3.67	1.89	1.88	1.37
Ni-N-HCNs-7h	1.89	2.54	1.07	1.08	0.59

Table S6. EXAFS data fitting results of Ni foil and Ni-N-HCNs-5h for Ni K-edge

Sample	Path	CN[a]	R (Å)[b]	σ^2 (Å²)[c]	$\Delta E0$ (eV)[d]	R factor
Ni foil	Ni-Ni	12	2.485 ± 0.001	0.0059	7.9	0.0009
Ni-N-HCNs-5h	Ni-N	3.2 ± 0.3	2.050 ± 0.006	0.0083	-2.8	0.0062
	Ni-N-C	2.8 ± 0.6	2.983 ± 0.019	0.0228	9.2	

[a]CN, coordination number; [b]R, the distance between absorber and backscatter atoms; [c]σ^2, the Debye-Waller factor value; [d]ΔE_0, inner potential correction to account for the difference in the inner potential between the sample and the reference compound; R factor indicates the goodness of the fit. $S0^2$ was fixed to 0.850, according to the experimental EXAFS fit of Ni foil, by fixing CN as the known crystallographic value. * This value was fixed during EXAFS fitting based on the known structure of Ni. Fitting conditions: k range：2.0 - 10.0; R range: 1.0-3.0; fitting space: R space; k-weight = 3. A reasonable range of EXAFS fitting parameters: 0.800 < S_0^2 < 1.000; CN > 0; σ^2 > 0 Å²; $|\Delta E_0|$ < 10 eV; R factor < 0.02.

Table S7. The content of various elements quantified by XPS for Ni-N-HCNs-5h prepared by different pyrolysis temperatures and different range of C$_3$N$_4$.

Example	C (wt.%)	N (wt.%)	O (wt.%)	Ni (wt.%)
700 ℃-1:15	75.49	15.26	6.73	2.52
800 ℃-1:10	79.23	12.1	6.46	2.21
800 ℃-1:15	80.39	11.99	5.41	2.21
800 ℃-1:20	78.66	13.55	4.95	2.84
900 ℃-1:15	81.84	9.08	6.61	2.47

Table S8. The content of different configurations of nitrogen derived from N 1s XPS for Ni-N-HCNs-5h prepared by different pyrolysis temperatures and different range of C$_3$N$_4$.

Example	Pyridinic N (wt.%)	Metal N (wt.%)	Pyrrolic N (wt.%)	Graphitic N (wt.%)	Oxidized N (wt.%)
700 ℃-1:15	4.79	4.07	3.20	1.45	1.75
800 ℃-1:10	4.04	3.38	2.85	0.84	0.99
800 ℃-1:15	3.18	3.67	1.89	1.88	1.37
800 ℃-1:20	4.55	3.38	2.42	2.19	0.53
900 ℃-1:15	1.51	2.14	1.86	3.21	0.35

Table S9. Comparison of the electrocatalytic performance of our catalysts with other state-of-the-art Ni single-atom catalysts reported in the flow cell.

Catalysts	Potential (V)	CO FE (%)	CO current density (mA cm^{-2})	Electrolyte	Reference
Ni-N-HCNs-5h	-0.77	95.7	287.2	1.0 M KOH	Our work
	-0.92	95.8	383.3		
	-0.99	96.2	480.8		
	-1.17	96.2	577.4		
Ni@C$_3$N$_4$-CN	-0.93	90	300	1.0 M KHCO$_3$	[8]
Ni SA/PCFM	-1.0	88	308.4	0.5 M KHCO$_3$	[9]
Ni-NAC	-1.4	90	151 (total)	N/A	[10]
Ni-N$_4$/C-NH$_2$	-1.0	89.3	447.6	1.0 M KOH	[11]
Ni SAs-NCW	-1.16	60	74.5	1.0 M KOH	[12]
Ni@N-C	-1.07	80	430	1.0 M KOH	[13]
Ni-SACs	-1.4	90	350	1.0 M KCl	[14]
NiPc-B@CNT	-1.2	95	400	1.0 M KHCO$_3$	[15]
CA/N-Ni	-1.2	91	300	6.0 M KOH + 0.2 M Zn (Ac)$_2$	[16]
Ni-N-C	-1.0	85	200	1.0 M KHCO$_3$	[17]
Ni-N3-NCNFs	-0.8	94	56.4	1.0 M KHCO$_3$	[18]
Ni (NC)-1	-1.82	99	160	1.0 M KOH	[19]

References

1. F. Xu, Z. Tang, S. Huang, L. Chen, Y. Liang, W. Mai, H. Zhong, R. Fu and D. Wu, *Nat. Commun.*, 2015, **6**, 7221.
2. J. Timoshenko and A. Kuzmin, *Comput. Phys. Commun.*, 2009, **180**, 920-925.
3. B. Ravel and M. Newville, *Journal of Synchrotron Radiation*, 2005, **12**, 537-541.
4. S. I. Zabinsky, J. J. Rehr, A. Ankudinov, R. C. Albers and M. J. Eller, *Physical Review B*, 1995, **52**, 2995-3009.
5. G. Kresse and D. Joubert, *Physical Review B*, 1999, **59**, 1758-1775.
6. J. P. Perdew, K. Burke and M. Ernzerhof, *Phys. Rev. Lett.*, 1997, **78**, 1396-1396.
7. S. Grimme, J. Antony, S. Ehrlich and H. Krieg, *J. Chem. Phys.*, 2010, **132**.
8. Q. Wang, K. Liu, K. Hu, C. Cai, H. Li, H. Li, M. Herran, Y.-R. Lu, T.-S. Chan, C. Ma, J. Fu, S. Zhang, Y. Liang, E. Cortes and M. Liu, *Nat. Commun.*, 2022, **13**.
9. H. Yang, Q. Lin, C. Zhang, X. Yu, Z. Cheng, G. Li, Q. Hu, X. Ren, Q. Zhang, J. Liu and C. He, *Nat. Commun.*, 2020, **11**, 593.
10. Z. C. Luo, Z. Y. Yin, J. Q. Yu, Y. Yan, B. Hu, R. F. Nie, A. F. Kolln, X. Wu, R. K. Behera, M. D. Chen, L. Zhou, F. D. Liu, B. Wang, W. Y. Huang, S. Zhang and L. Qi, *Small*, 2022, **18**, 2107799.
11. Z. Chen, X. Zhang, W. Liu, M. Jiao, K. Mou, X. Zhang and L. Liu, *Energy Environ. Sci.*, 2021, **14**, 2349-2356.
12. H. Chang, H. Pan, F. Wang, Z. Zhang, Y. Kang and S. Min, *Nanoscale*, 2022, **14**, 10003-10008.
13. Y. Liu, Z. Miao, M. Liang, J. Zhang, J. Zhao, L. Xu, J. Zhou and S. Zhuo, *Appl. Surf. Sci.*, 2023, **614**.
14. Q. Fan, P. Gao, S. Ren, Y. Qu, C. Kong, J. Yang and Y. Wu, *Nano Res.*, 2022, DOI: 10.1007/s12274-022-4472-6.
15. Y. Huang, H. Dai, D. Moonshiram, Z. Li, Z.-M. Luo, J.-H. Zhang, W. Yang, Y. Shen, J.-W. Wang and G. Ouyang, *J. Mater. Chem. A*, 2023, **11**, 2969-2978.
16. Y. Zhang, X. Wang, S. Zheng, B. Yang, Z. Li, J. Lu, Q. Zhang, N. M. Adli, L. Lei, G. Wu and Y. Hou, *Adv. Funct. Mater.*, 2021, **31**.
17. T. Möller, W. Ju, A. Bagger, X. Wang, F. Luo, T. Ngo Thanh, A. S. Varela, J. Rossmeisl and P. Strasser, *Energy Environ. Sci.*, 2019, **12**, 640-647.
18. W. Zheng, Y. Wang, L. Shuai, X. Wang, F. He, C. Lei, Z. Li, B. Yang, L. Lei, C. Yuan, M. Qiu, Y. Hou and X. Feng, *Adv. Funct. Mater.*, 2021, **31**.
19. C. F. Wen, F. Mao, Y. Liu, X. Y. Zhang, H. Q. Fu, L. R. Zheng, P. F. Liu and H. G. Yang, *ACS. Catal.*, 2020, **10**, 1086-1093.